ESTIMATING WATER SATURATION AT THE GEYSERS BASED ON HISTORICAL PRESSURE AND TEMPERATURE PRODUCTION DATA AND BY DIRECT MEASUREMENT

FINAL REPORT TO CALIFORNIA ENERGY COMMISSION

PIER GRANT PIR-00-004

JUNE 2003

ROLAND N. HORNE

JERICHO L.P. REYES

KEWEN LI

Stanford Geothermal Program

Abstract

Available historical data from 503 wells at the Geysers geothermal field were analyzed to estimate in-situ water saturation using zero-dimensional models in the reservoir. The pressure and temperature performance data of most of the wells demonstrate "dry-out" due to the formation of superheated steam. The in-situ water saturation of the reservoir can be inferred by using zero-dimensional models derived from mass and energy conservation equations. Techniques to identify the initial reservoir temperature and the dry-out temperature were developed and used in the saturation calculations. Effects of reinjection of the Geysers were analyzed and compared to models of depleted reservoirs. Regional trends of the saturation values plotted in the Cartesian plane were also investigated.

An experimental apparatus was also designed and built to directly measure the in-situ steam and water saturations in The Geysers rock by using an X-ray CT technique. Water saturation was measured at a temperature of about 120^{o}C but at different pressures. The pressure in the core sample ranged from 0 to about 50 psi. The experimental data from The Geysers rock were also compared to the theoretical results from a zero-dimensional model. X-ray beam-hardening effects are frequently reduced by the installation of core systems in water jackets or in sand packs. Such a method may not be convenient and may not work in some cases. A new approach was developed to measure fluid saturations by inclining the core to the scanning plane to reduce X-ray beam-hardening effects.

Acknowledgments

This work was funded by a PIER Grant by the California Energy Commission. We are also grateful for the assistance of the California Division of Oil, Gas and Geothermal Resources and Calpine Corporation in obtaining field data.

Contents

Abstract iii

Acknowledgments v

Contents vii

List of Tables ix

List of Figures xi

1. Introduction 1

2. Estimation of In-situ Saturation using Production Data 3

    2.1. Geysers Database 3
    2.2. Previous Results in Simulation and Modeling 6
        2.2.1. Zero-Dimensional Model 7
        2.2.2. TOUGH2 Two-Phase Radial Flow Model 7
    2.3. Numerical Simulation of Pressure-Temperature Profiles 9
    2.4. Estimation of the Initial Reservoir Temperature 14
    2.5. Estimation of Dry-out Temperature 15

3. Estimated In-Situ Saturation Results 21

    3.1. Evaluation of Temperature 21
    3.2. Evaluation of Other Properties 23
    3.3. Calculation of Saturation Values 24
    3.4. Other Wells 29

4. Direct Measurement of the In-Situ Saturation 32

    4.1. Method 32
    4.2. Experiments 33
    4.3. Results 37
    4.4. Discussion 41

5. Effect of Reinjection 42

    5.1. Simulation of Reinjection 42
    5.2. Effect of Reinjection Location 43
    5.3. Effect of Reinjection Flowrate 44

6. Conclusions 46

Nomenclature 47

References 49

List of Tables

Table 2-1: Reservoir properties used in the simulation. 7

Table 3-1: In-situ saturation values calculated from various porosity values.................. 24

Table 3-2: Calculated in-situ saturation values for 177 wells in The Geysers database... 25

Table 5-1: Effect of location of reinjection well to the in-situ water saturation value. 44

Table 5-2: Effect of flowrate of the reinjection well to the in-situ water saturation value. 44

List of Figures

Figure 2-1: Pressure-temperature profile of the McKinley 1 well. 4

Figure 2-2: Pressure-temperature profile of the Thorne 1 well.. 4

Figure 2-3: Temperature and pressure history for the McKinley 1 well. 5

Figure 2-4: Temperature and pressure history for the Thorne 1 well. 6

Figure 2-5: Production enthalpy and reservoir temperature profiles: initial water saturation = 0.3, irreducible water saturation = 0.3 (Belen, 2000). 8

Figure 2-6: Production enthalpy and reservoir temperature profiles: initial water saturation = 0.2, irreducible water saturation = 0.2 (Belen, 2000). 9

Figure 2-7: Pressure-temperature profile of the TOUGH2 simulated model, irreducible water saturation = 0.3. 10

Figure 2-8: Pressure-temperature profile of the TOUGH2 simulated model, irreducible water saturation = 0.2. 10

Figure 2-9: Temperature and pressure history for the TOUGH2 simulated model, irreducible water saturation = 0.3. 11

Figure 2-10: Temperature and pressure history for the TOUGH2 simulated model, irreducible water saturation = 0.2. 12

Figure 2-11: Temperature values over a 315 year exploitation period for the TOUGH2 simulated two-phase radial model, irreducible water saturation = 0.3, with initial temperature, T_o and dry-out temperature, T_d indicated. 13

Figure 2-12: Estimation of the initial reservoir temperature T_o, using a median sample window of 5 months for McKinley 1. The estimated T_o is 201.5 ºC. 14

Figure 2-13: Estimation of the initial reservoir temperature T_o, using a median sample window of 5 months for Thorne 1. The estimated T_o is 199 ºC. 15

Figure 2-14: Correlation between temperature and pressure data points for McKinley 1. 16

Figure 2-15: Correlation between temperature and pressure data points for Thorne 1..... 16

Figure 2-16: Saturated pressure values calculated from well temperature values and pressure values for the McKinley 1 well. 17

Figure 2-17: Saturated pressure values calculated from well temperature values and pressure values for the Thorne 1 well. 18

Figure 2-18: Plot of ln(p) vs. 1/T based on the Clausius-Clapeyron Equation. 19

Figure 2-19: Plot of ln(p) vs. 1/T of the McKinley 1 pressure and temperature values to determine the dry-out temperature. The estimated T_d is 193.2 ºC. 19

Figure 2-20: Plot of ln(p) vs. 1/T of the Thorne 1 pressure and temperature values to determine the dry-out temperature. The estimated T_d is 197.6 ºC. 20

Figure 3-1: Wellhead and wellbore temperatures for McKinley 1 well. 22

Figure 3-2: Wellhead and wellbore temperatures for Thorne 1 well. 23

Figure 3-3: Aerial view contour plot of the saturation values on the Cartesian plane of the 177 superheated Geyser wells. 29

Figure 3-4: Temperature and pressure values history for a well with no dry-out point. 30

Figure 3-5: Pressure-temperature profile of a well with sparse data. 31

Figure 3-6: : Locations of the saturated wells. 31

Figure 4-1: Schematic of the apparatus used to measure in-situ water saturation. 33

Figure 4-2: Schematic of the aluminum coil used to control the temperature in the core. 34

Figure 4-3: Picture of the core and core holder system prior to wrapping insulation material. 35

Figure 4-4: Picture of back view of the apparatus. 36

Figure 4-5: Picture of the whole apparatus used to measure in-situ water saturation. 36

Figure 4-6: CT image obtained by scanning the core sample in the longitudinal direction. 38

Figure 4-7: CT image obtained by scanning the core sample inclined to the longitudinal direction. 38

Figure 4-8: Effect of temperature on the CT value of the core sample saturated with water. 39

Figure 4-10: Variation of in-situ water saturation in The Geysers rock with pressure at a temperature of 120^{o}C. 40

Figure 5-1: Locations of the injection wells. 42

Figure 5-2: Pressure-temperature history showing the dry-out point for a simulation run showing reinjection. 43

Figure 5-3: Production well and reinjection well locations in the simulation model. 44

Chapter 1

1. Introduction

The Geysers geothermal field in Northern California is the largest producing vapor-dominated field in the world. The exploitation of the geothermal reservoir entails the extraction of thermal energy, which is then used to generate electricity. Accurate knowledge of the parameters involved in this recovery process is of substantial economic value in making most effective use of the resource.

Exploitation of a geothermal field is dependent on the quantity of heat available in the reservoir and on how long it can be extracted (Bowen, 1989). Recovery of energy from a geothermal reservoir requires that mass be withdrawn from it. Once a reservoir has reached its maximum exploitative capacity, no more fluid can be extracted unless additional recharge liquid is injected into the reservoir artificially. Understanding when fluid will be exhausted and how much remains at any moment are important to predicting the ultimate recovery of the resource.

The basic components of a vapor-dominated geothermal reservoir are its reserves of steam and immobile water. Under exploitation the vapor-dominated field can be locally depleted of water to form a dry or superheated zone. There is a recharge of steam from boiling of the immobile water. Even though the steam is the principal recovery fluid, by mass the immobile water represents a much larger component of the reservoir fluid than the steam. Hence quantifying the immobile water in the reservoir is of particular importance.

Knowledge of the immobile and in-situ water saturation will also provide better understanding of the fluid storage capacities of geothermal rocks, as this is valuable in estimating the performance of a geothermal reservoir and its capacity for further exploitation.

Past projects have relied on numerical simulation to infer field conditions. Similar techniques have also been used to infer flow and saturation properties from experimental measurements. Belen and Horne (2000) used numerical simulation to verify values of in-situ and immobile water saturations calculated from zero-dimensional models based on those described in Grant, Donaldson and Bixley (1982). The principal objective of this study was to use Belen's model to match field data from The Geysers and thereby estimate the immobile water saturation.

These studies used numerical simulation to verify and extend present field measurements or experimental values. Numerical simulation provides a means to predict and visualize the performance of a certain system under known parameters (Pruess, 1991). Simulating a geothermal reservoir's behavior during exploitation allows us to infer reservoir parameters, forecast future performance and design optimal development strategy.

Chapter 2

2. Estimation of In-situ Saturation using Production Data

2.1. Geysers Database

The Geysers Geothermal Field is located in Northern California about 130 km north of San Francisco. Since 1987, The Geysers has experienced a decline in steam pressure (Barker and Pingol, 1997). Recovering some of the reduced reservoir capacity has been achieved by injecting water into parts of The Geysers reservoir to recover additional heat.

The Geysers production database was made available by the California Division of Oil, Gas and Geothermal Resources. The Geysers database, which contains temperature and pressure values for 502 wells around The Geysers field area, also contains information on the history and overall structure of the wells. As an illustrative example, this report will describe two wells from The Geysers database, namely McKinley 1 and Thorne 1, located in the Lake and Sonoma Counties. McKinley 1, a redrilled active producer well owned by the Calpine Geysers Company, had a depth of 2219.18 feet. Thorne 1, also an active producer well, has a depth of 6842 feet.

The pressure-temperature profiles of the wells, gathered over a period of 20 years, are plotted against the steam saturation curve and shown in Figure 2-1 and Figure 2-2.

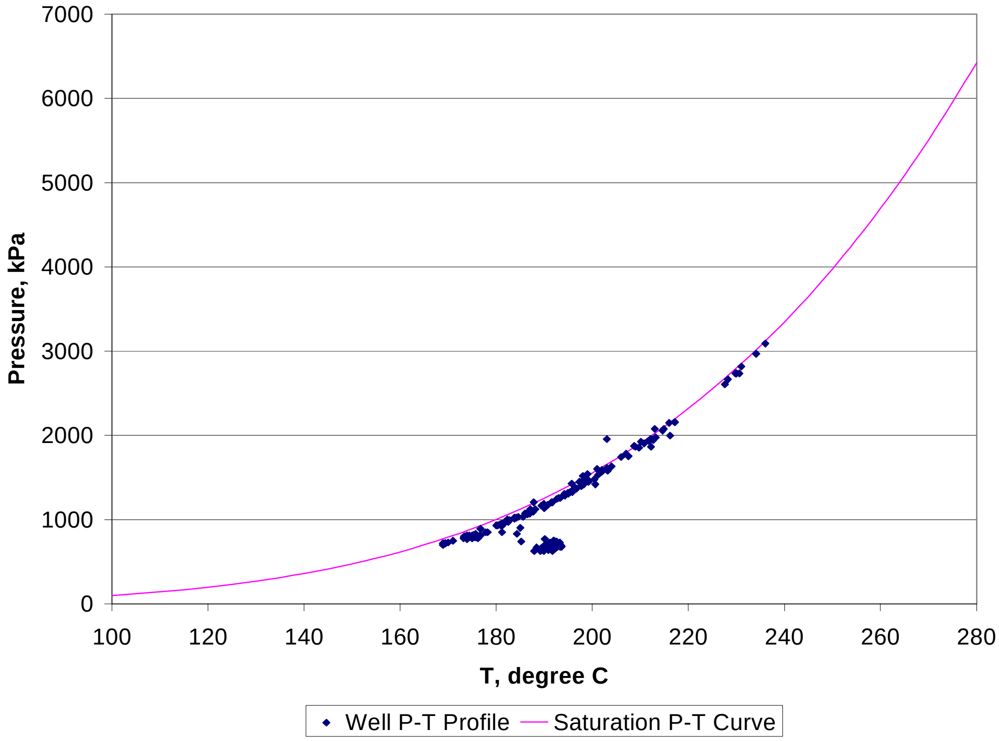

Figure 2-1: Pressure-temperature profile of the McKinley 1 well.

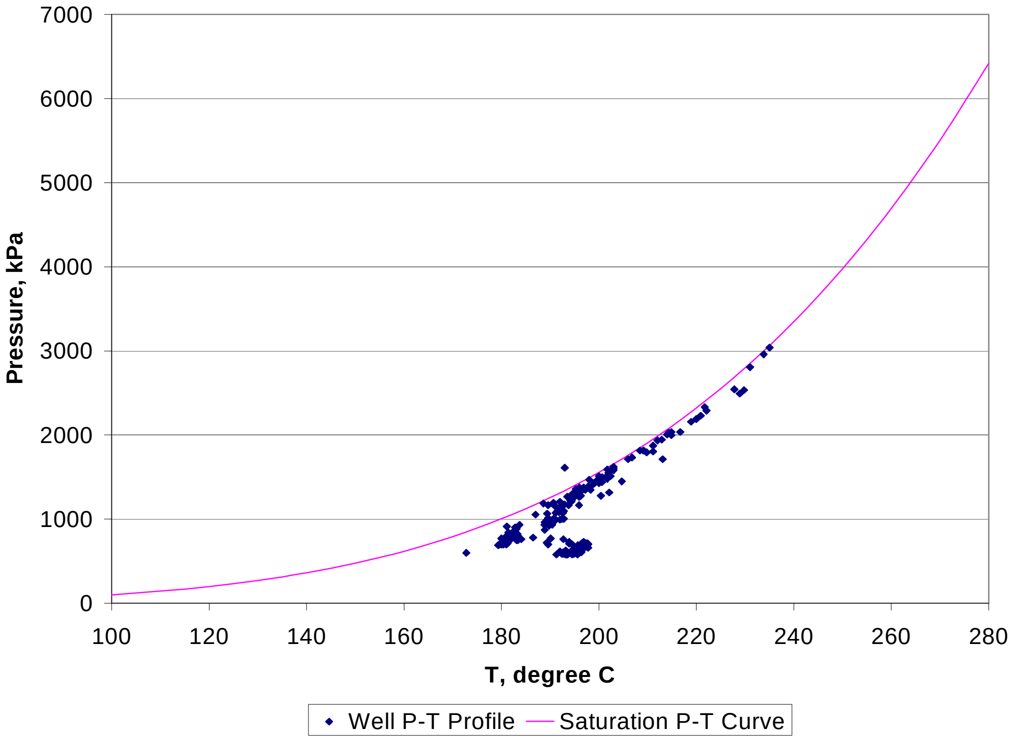

Figure 2-2: Pressure-temperature profile of the Thorne 1 well.

The well pressure-temperature profiles suggest a clear relationship with the saturation pressure temperature curve of water. A noticeable deviation is the formation of a cluster at the lower pressure values under the saturation curve. The formation of this “elbow” in the pressure-temperature profile, in which the pressure values are lower than the saturated values for a certain temperature, can be attributed to the point in the exploitation history at which the immobile saturation of the water in the reservoir has been boiled away. The immobile saturation of the water is liquid that cannot flow in the reservoir, and hence represents an “invisible” phase. Nonetheless, the immobile water will become steam during exploitation, due to boiling, and hence is a very important source of energy.

To better understand when this phenomenon happens, we plotted the histories of the well over the same 20-year span. The result is shown in Figure 2-3 and Figure 2-4.

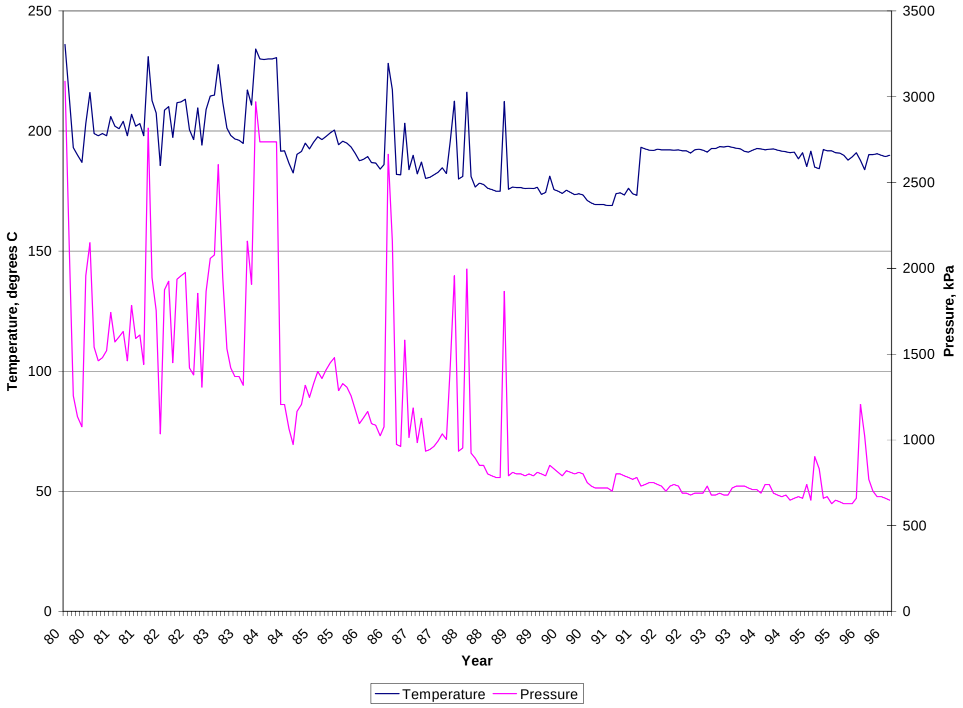

Figure 2-3: Temperature and pressure history for the McKinley 1 well.

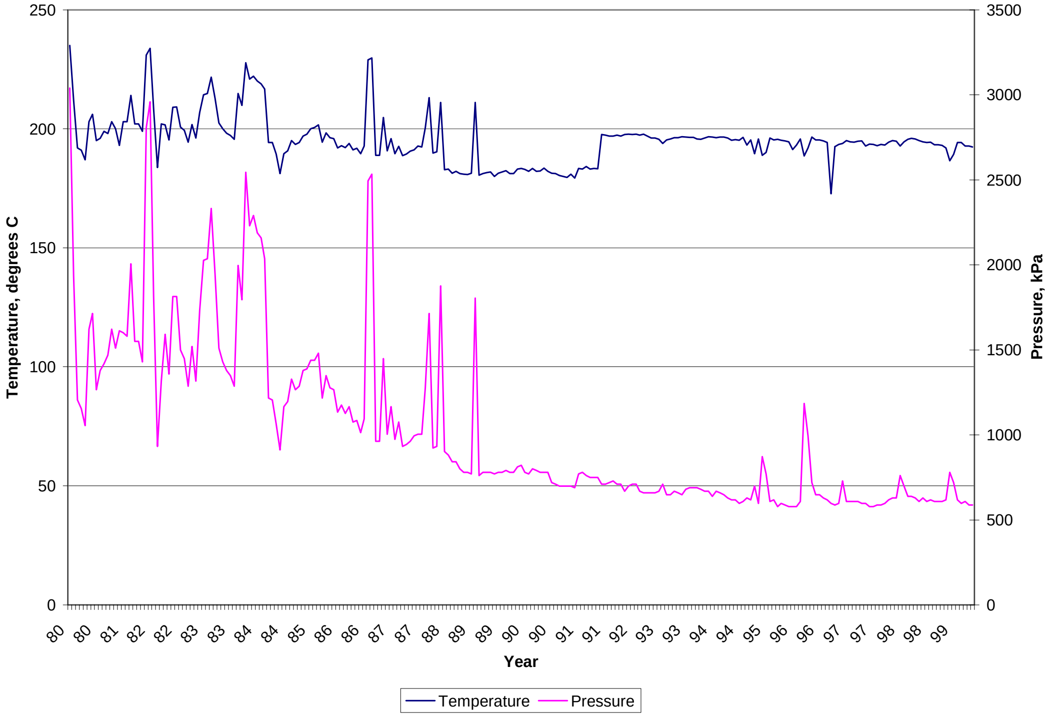

Figure 2-4: Temperature and pressure history for the Thorne 1 well.

It can be seen in the left side of Figure 2-3 that the temperature fluctuates in the same manner as the pressure, or when the pressure goes up, the temperature goes up too. This trend is noticed from years 1980 to 1991. After a brief leveling off, the trend goes the opposite way, or when the temperature goes down, the pressure goes up and vice versa. Whether or not these phenomena are attributable to the point in the reservoir exploitation where the immobile water saturation has boiled away is examined in the following sections. Similar trends can be seen in Figure 2-4.

2.2. Previous Results in Simulation and Modeling

In order to generate similar curves for temperature and pressure of a producer well under exploitation, we need to produce numerical models to simulate the geothermal reservoir under exploitation. This will allow us to investigate whether the elbow in the pressure-temperature profile is indeed because the reservoir has boiled away the immobile water saturation.

In 2000, Belen developed a two-phase radial reservoir model to determine the end-point saturation of steam and liquid water relative permeability curves by inference from pressure, temperature and saturation data. The objective of the study was to determine the end-points based on both zero-dimensional models and from numerical simulation.

2.2.1. *Zero-Dimensional Model*

Geothermal reservoirs under exploitation can be modeled using zero-dimensional models derived from material and energy conservation equations and Darcy's Law. Using the characteristics of vapor-dominated reservoirs, which primarily is the classification of The Geysers, where the mobile phase is steam, Darcy's Law describes the steam flow.

$$\phi \frac{\partial}{\partial t}\{s\rho_w + (1-s)\rho_s\} = -\nabla \cdot (\vec{u}_s \rho_s) \tag{2-1}$$

$$\frac{\partial}{\partial t}\{(1-\phi)\rho_r c_r T + \phi(1-s)\rho_s h_s\} = -\nabla \cdot (\vec{u}\rho_s h_s) \tag{2-2}$$

$$\vec{u} = \frac{kk_{rs}}{\mu_s}\nabla p \tag{2-3}$$

The enthalpy of saturated steam is nearly constant with temperature under reservoir conditions. This allows the simplification of the energy conservation equation relating pressure and saturation.

$$(1-\phi)\rho_r C_r T + \phi s \rho_w (h_w - h_s) = \text{constant} \tag{2-4}$$

Belen (2000) derived a zero-dimensional model that allows us to calculate the in-situ water saturation using rock and fluid properties,

$$s_o = \frac{(1-\phi)}{\phi}\frac{\rho_r c_r (T_o - T_d)}{\rho_w (h_s - h_w)\big|_{T_o}} \tag{2-5}$$

where T_o is the initial reservoir temperature and T_d is the dry-out temperature.

2.2.2. *TOUGH2 Two-Phase Radial Flow Model*

A two-phase radial flow was modeled using the numerical simulator TOUGH2 (Pruess, 1991). A cylindrical model was used in the simulation runs. A single well was placed in the middle of the reservoir. Table 2-1 summarizes the parameters used for the runs.

Table 2-1: Reservoir properties used in the simulation.

Porosity	5%
Permeability	1×10^{-13} m^2
Rock Density	2600 kg / m^3
Rock Specific Heat	485 J / kg ºC
Reservoir Radius	1000 m
Reservoir Thickness	10 m
Initial Reservoir Temperature	280 ºC

The model consisted of 100 grid blocks, with grid size increasing logarithmically from the center to the boundary of the reservoir.

Figure 2-5 compares the production enthalpies simulated by TOUGH2 with those predicted by the zero-dimensional model with in-situ water saturation of 0.3. There is good agreement between the simulator and the model results. Figure 2-6 shows another vapor-dominated case, this time with a higher in-situ saturation to 0.3.

In these two cases, the zero-dimensional model simulated reservoir temperatures satisfactorily in comparison to the values computed with TOUGH2. Therefore, it is reasonable to use the zero-dimensional model to analyze the data taken from actual wells in The Geysers geothermal field. It should be noted that the ability of a volume-averaged model to replicate the fully dimensional result justifies the application to The Geysers, which is admittedly a heteregoneous and fractured reservoir. The pressure-temperature history data from the Geysers is analyzed over long periods (e.g. 20 years), during which time the bulk behavior is not expected to be governed by fractures and heterogeneities.

The study concluded that both in-situ and immobile water saturations could be inferred from field measurements using simple zero-dimensional models and TOUGH2 two-phase radial flow simulation results.

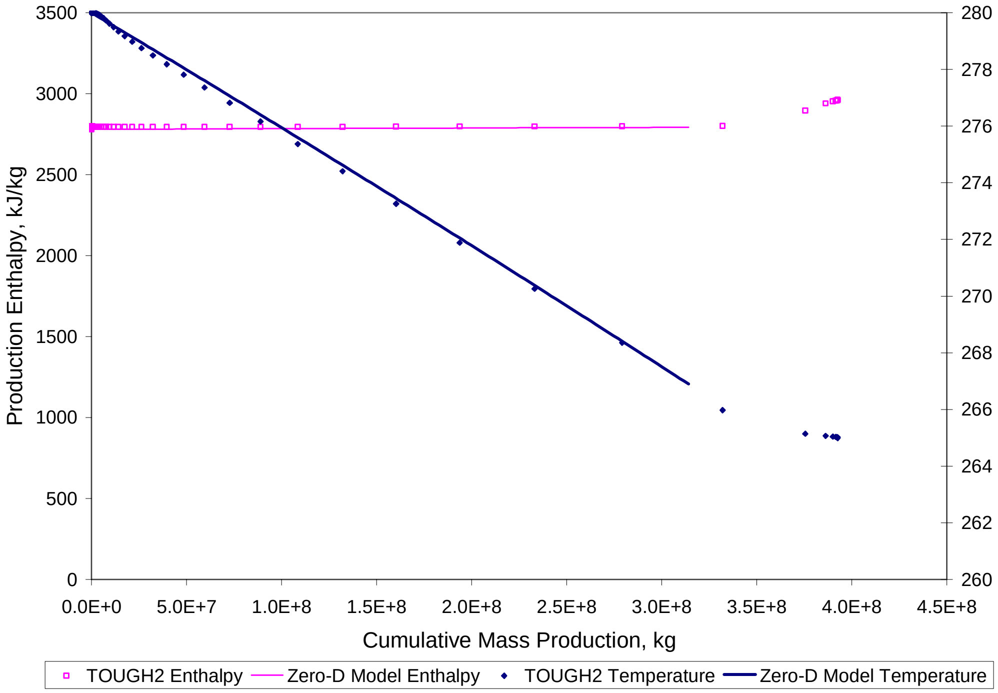

Figure 2-5: Production enthalpy and reservoir temperature profiles: initial water saturation = 0.3, irreducible water saturation = 0.3 (Belen, 2000).

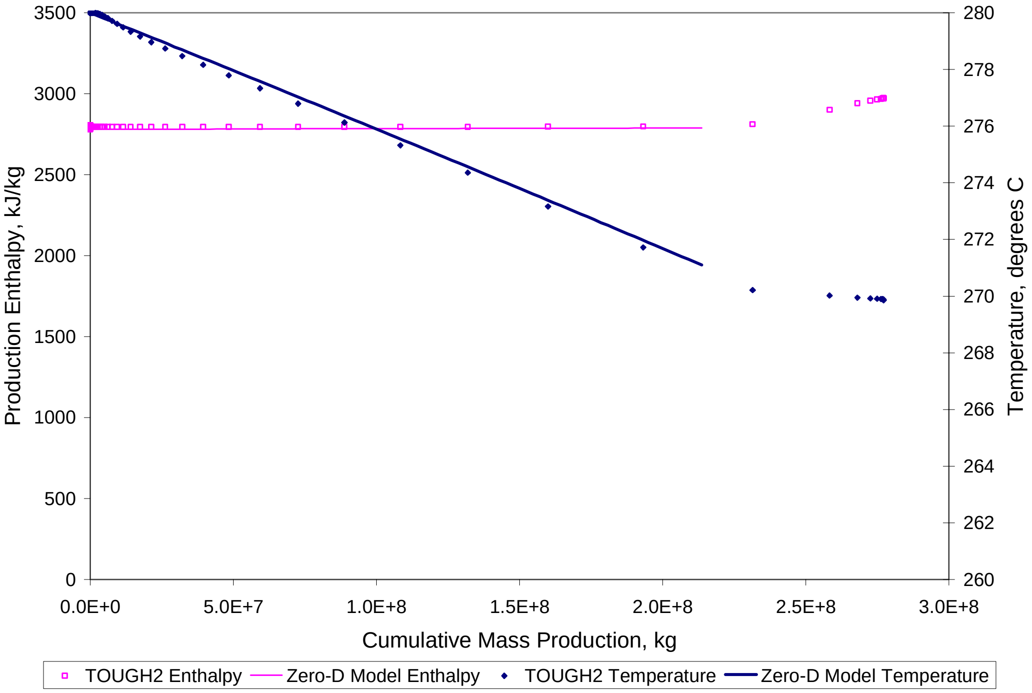

Figure 2-6: Production enthalpy and reservoir temperature profiles: initial water saturation = 0.2, irreducible water saturation = 0.2 (Belen, 2000).

2.3. Numerical Simulation of Pressure-Temperature Profiles

Using the two-phase radial model developed by Belen (2000), and using the parameters given in Table 2-1, TOUGH2 simulations were made and pressure-temperature profiles were plotted. These plots are shown in Figure 2-7 and Figure 2-8, with irreducible water saturation taken as 0.3 and 0.2 respectively.

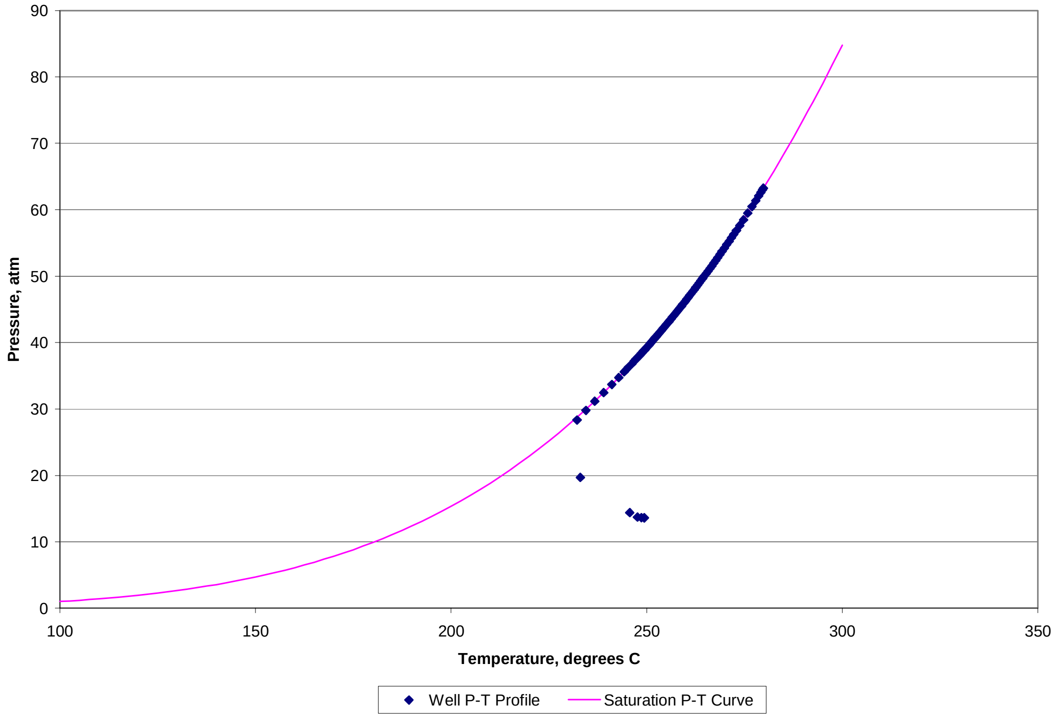

Figure 2-7: Pressure-temperature profile of the TOUGH2 simulated model, irreducible water saturation = 0.3.

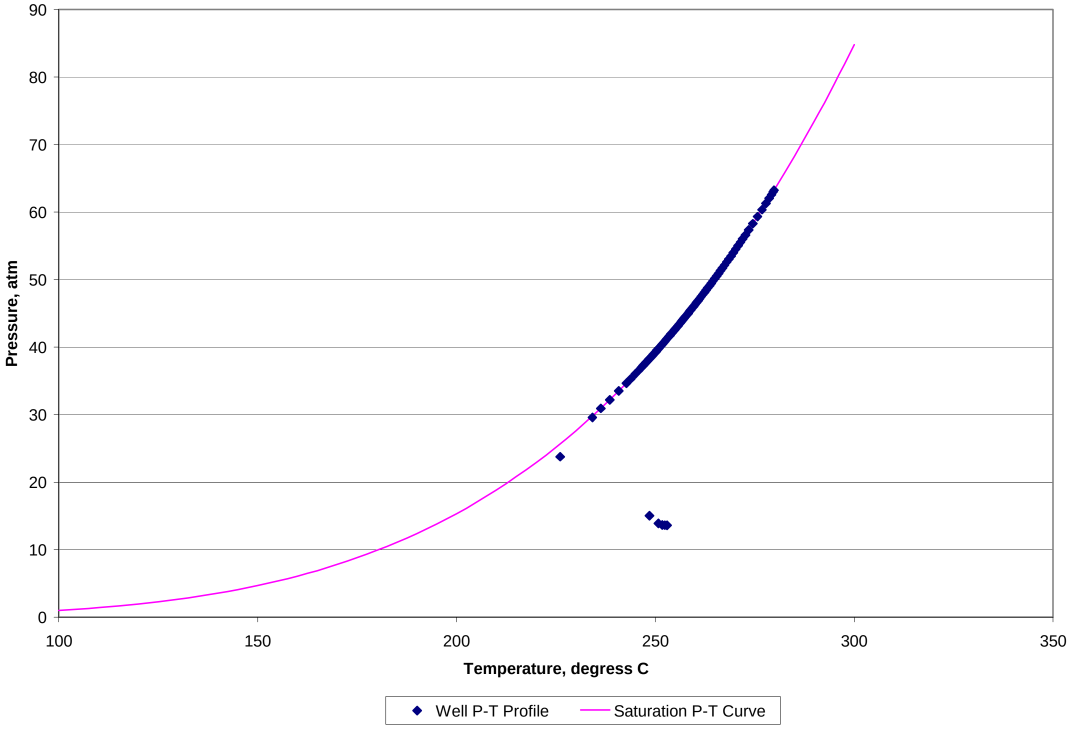

Figure 2-8: Pressure-temperature profile of the TOUGH2 simulated model, irreducible water saturation = 0.2.

The simulated values follow the saturation curve, with the appearance of an elbow, similar to the data seen in wells McKinley 1 and Thorne 1. The simulation shows that when the reservoir reaches zero saturation, a lowering of pressure is observed as the well zone becomes superheated. Pressure values decrease and deviate from the saturation curve.

The history of the exploitation of the simulated reservoir is plotted in Figure 2-9 and Figure 2-10 for 0.3 and 0.2 values of in-situ water saturation, respectively, to better understand at what point this elbow occurs and if it is comparable with the actual well histories plotted in Figure 2-3 and 2-4.

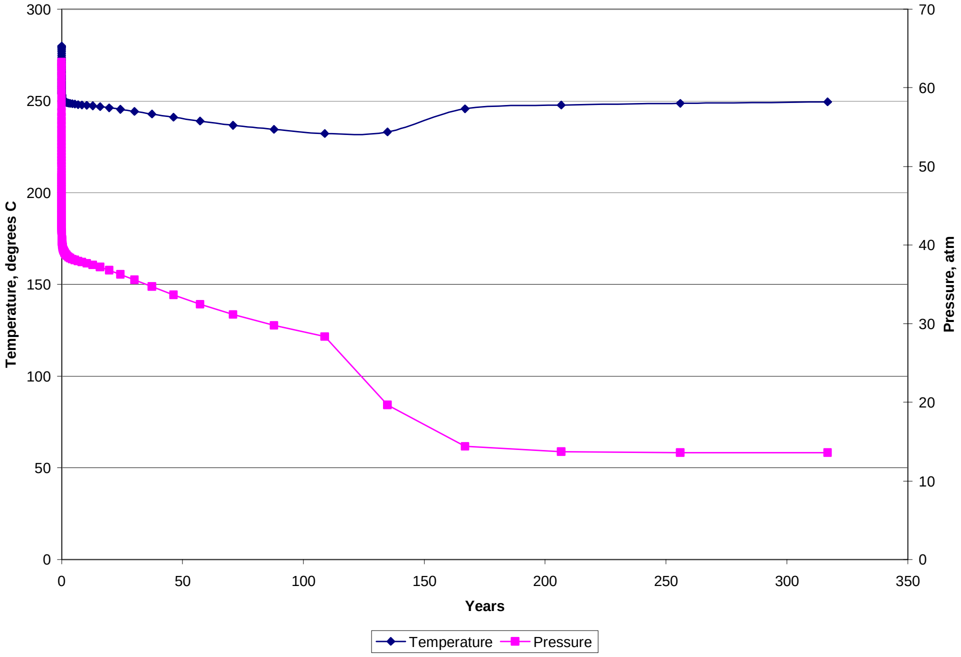

Figure 2-9: Temperature and pressure history for the TOUGH2 simulated model, irreducible water saturation = 0.3.

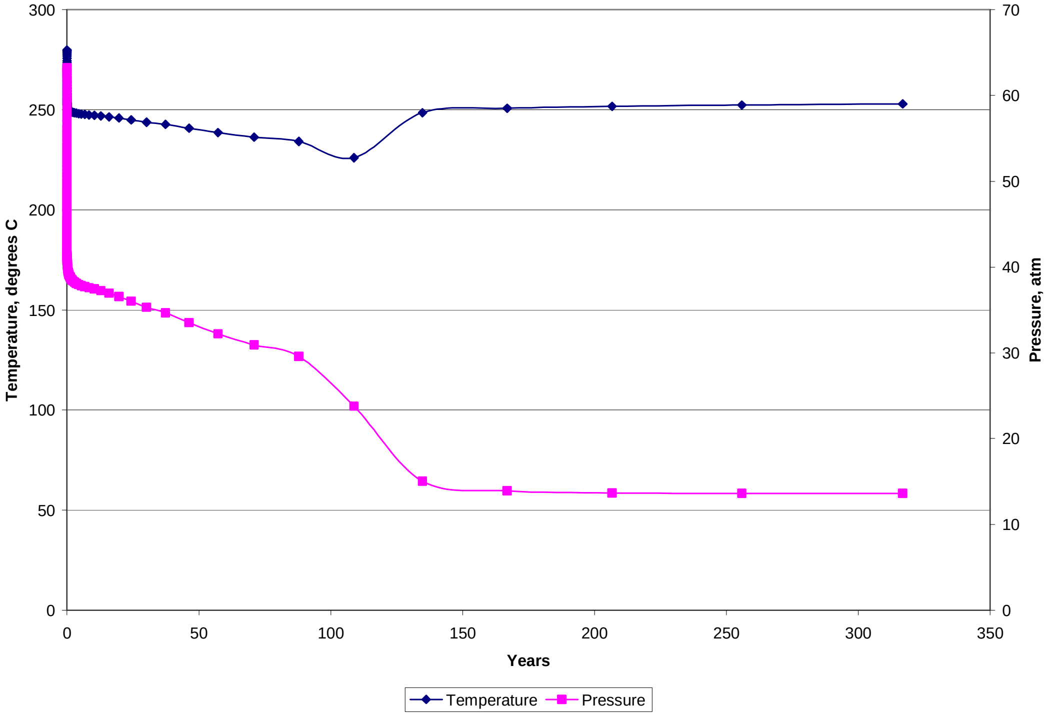

Figure 2-10: Temperature and pressure history for the TOUGH2 simulated model, irreducible water saturation = 0.2.

For both graphs, the temperature and pressure histories from 0 to 100 years are in direct relationship, that is, when pressure decreases, the temperature also decreases. After that, however, the opposite relationship exists, or as the temperature goes up, the pressure goes down. The point at which the behavior changes corresponds to the formation of the elbow in Figure 2-7 and Figure 2-8, and is indicative of the reservoir reaching zero water saturation. This confirms the proposed explanation of the behavior of the McKinley 1 and Thorne 1 wells, which showed a similar phenomenon.

To verify these results, we calculated the in-situ water saturation for the simulation run using Equation 2-5. From the equation, it is seen that two temperatures are needed for the calculation of s_o. The initial reservoir temperature, T_o, is used to evaluate the fluid properties ρ_w, h_s and h_w. The dry-out temperature, T_d, is determined to be the temperature just before the well reaches s_o. These two temperatures are indicated in Figure 2-11 for the $s_o = 0.3$ run.

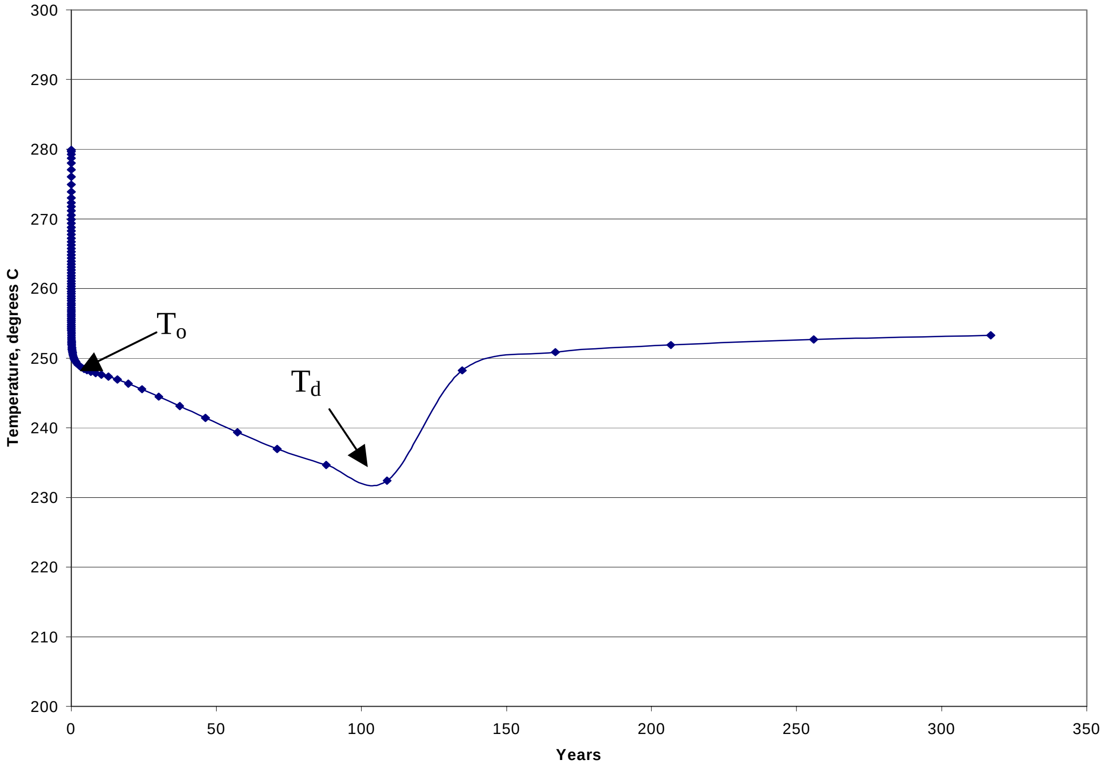

Figure 2-11: Temperature values over a 315 year exploitation period for the TOUGH2 simulated two-phase radial model, irreducible water saturation = 0.3, with initial temperature, T_o and dry-out temperature, T_d indicated.

The zero-dimensional model, as expressed in Equation 2-5 with reservoir properties used in Table 2-1, gives a close approximation of the in-situ water saturation used in the simulation. This means that the assumptions taken in the zero-dimensional model can closely approximate the conditions in actual geothermal wells, therefore, this method is useful to calculate the in-situ water saturation in the Geyser wells.

Using the T_o and T_d values from Figure 2-9:

$$s_o = \frac{(1-\phi)}{\phi}\frac{\rho_r c_r (T_o - T_d)}{\rho_w (h_s - h_w)\big|_{T_o}} = \frac{(1-0.05)}{0.05}\frac{\left(2600\,{}^{kg}\!/_{m^3}\right)\left(0.485\,{}^{kJ}\!/_{kgC}\right)\left(250^o C - 232^o C\right)}{799.1689\,{}^{kg}\!/_{m^3}\left(2800.4\,{}^{kJ}\!/_{kg} - 1085.78\,{}^{kJ}\!/_{kg}\right)} = 0.31$$

Using the T_o and T_d values from Figure 2-10:

$$s_o = \frac{(1-\phi)}{\phi}\frac{\rho_r c_r (T_o - T_d)}{\rho_w (h_s - h_w)\big|_{T_o}} = \frac{(1-0.05)}{0.05}\frac{\left(2600\,{}^{kg}\!/_{m^3}\right)\left(0.485\,{}^{kJ}\!/_{kgC}\right)\left(246^o C - 233^o C\right)}{805.1\,{}^{kg}\!/_{m^3}\left(2801.36\,{}^{kJ}\!/_{kg} - 1066.42\,{}^{kJ}\!/_{kg}\right)} = 0.22$$

2.4. Estimation of the Initial Reservoir Temperature

Figure 2-3 and Figure 2-4 show that, with the temperature-pressure profile of The Geysers wells, unlike with the simulated results, the initial reservoir temperature, *T_o*, cannot be distinguished so easily. Taking into account the initial sudden drop in the downhole wellbore pressure as a response to production, the stable temperature, *T_o*, after the early transient period can be estimated by taking the median temperatures in the first few years. Figures 2-12 and 2-13 illustrate this estimation.

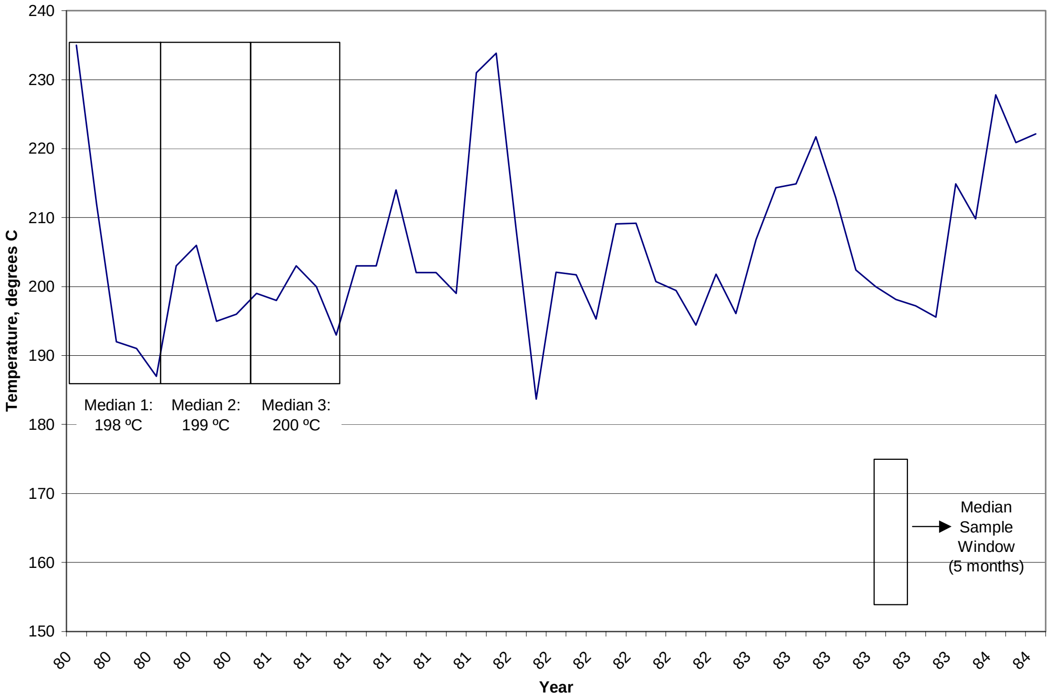

Figure 2-12: Estimation of the initial reservoir temperature T_o, using a median sample window of 5 months for McKinley 1. The estimated T_o is 201.5 ºC.

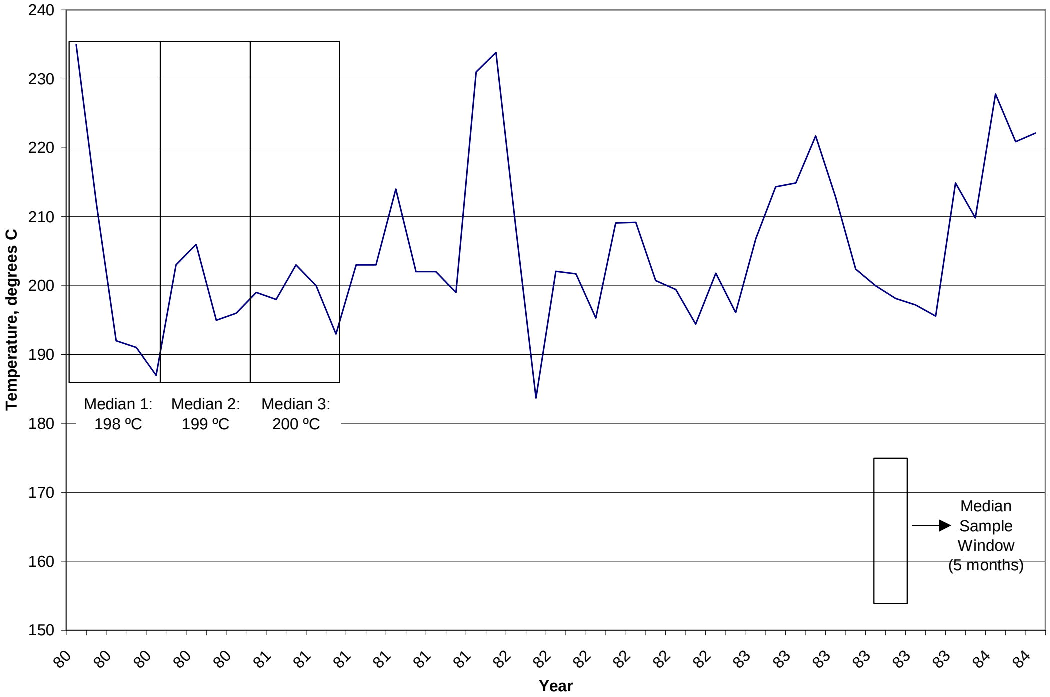

Figure 2-13: Estimation of the initial reservoir temperature T_o, using a median sample window of 5 months for Thorne 1. The estimated T_o is 199 ºC.

2.5. Estimation of Dry-out Temperature

The dry-out temperature can be estimated by acknowledging the fact that this temperature is found where the direct relationship of the temperature and pressure ends, and where the inverse relationship begins, as observed in the determination of the T_d in the simulation case. To see this, consider Figure 2-1 and Figure 2-2. The region of the pressure-temperature profile following the saturation curve corresponds to the period of direct relationship in the pressure and temperature values, and the values below the elbow correspond to the inverse relationship. Figures 2-14 and 2-15 illustrate the relationships that are present with pressure and temperature values, as seen in the computation of the correlation function *R*. using a five-point moving window. A correlation function value *R* of 1 signifies positive correlation, while an *R* of –1 signifies a negative correlation.

It can be seen from these figures that a good part of the left side of either graph has a generally positive correlation. The right side, on the other hand, fluctuates from positive to negative correlation, although the relationship is largely inverse.

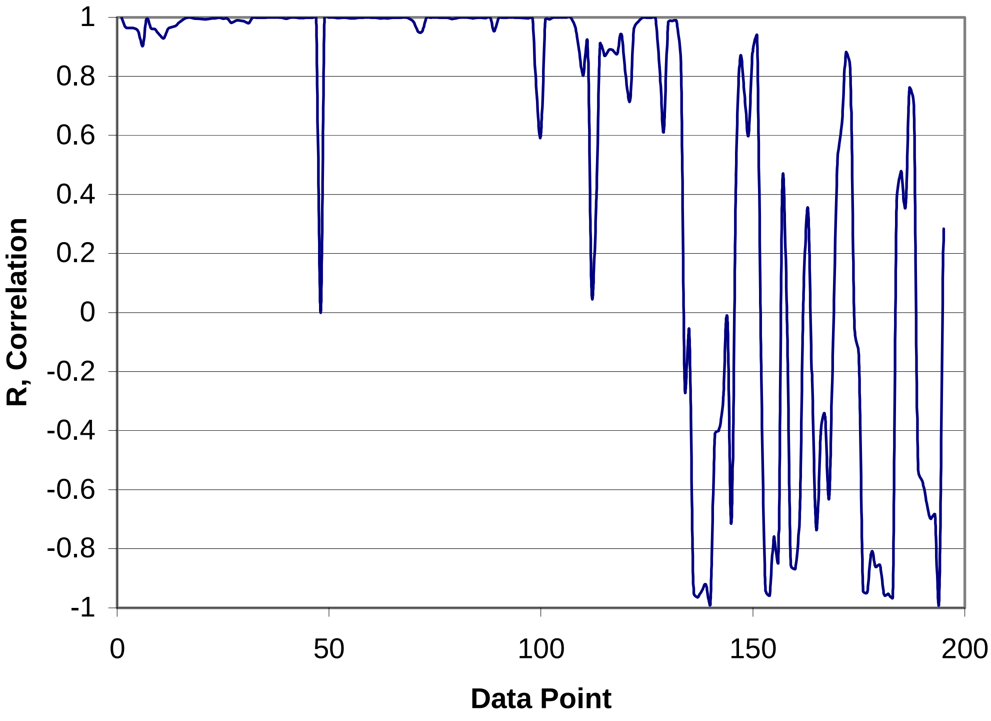

Figure 2-14: Correlation between temperature and pressure data points for McKinley 1.

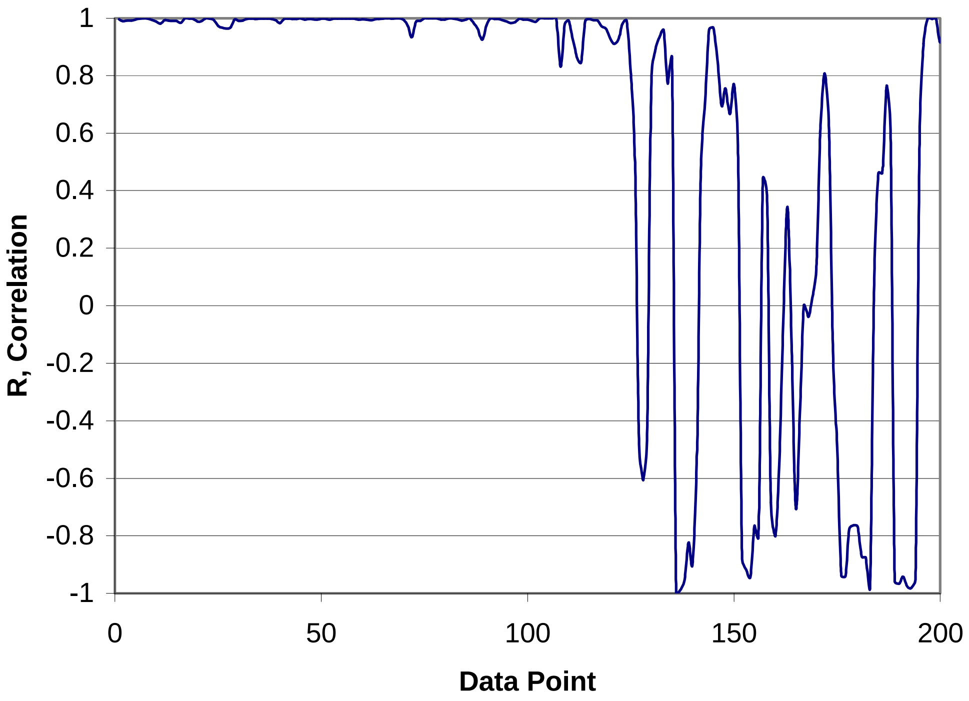

Figure 2-15: Correlation between temperature and pressure data points for Thorne 1.

We can estimate this transition point numerically by recognizing that, at the values of positive correlation, the temperature and pressure values obey the saturation curve. The saturation curve values are generated using the Clausius-Clapeyron equation, given by Equation 2-6.

$$\ln p = -\frac{\Delta h_{vap}}{R_g T} + C \tag{2-6}$$

This equation includes the Δh_{vap} , which is the heat of vaporization of water, and R_g, the universal gas constant. Therefore, we can estimate the time when the positive correlation zone ends, by analyzing the point at which the values of temperature and pressure history stop following the Clausius-Clapeyron equation.

Figures 2-16 and 2-17 show the plot of the saturation pressure values computed from the corresponding historic well temperature values, in comparison to the historic pressure well values. We can see that there are points at which the well pressure values start to deviate from the saturated values, as indicated by the arrows. These points can also be used to estimate the point of dry-out.

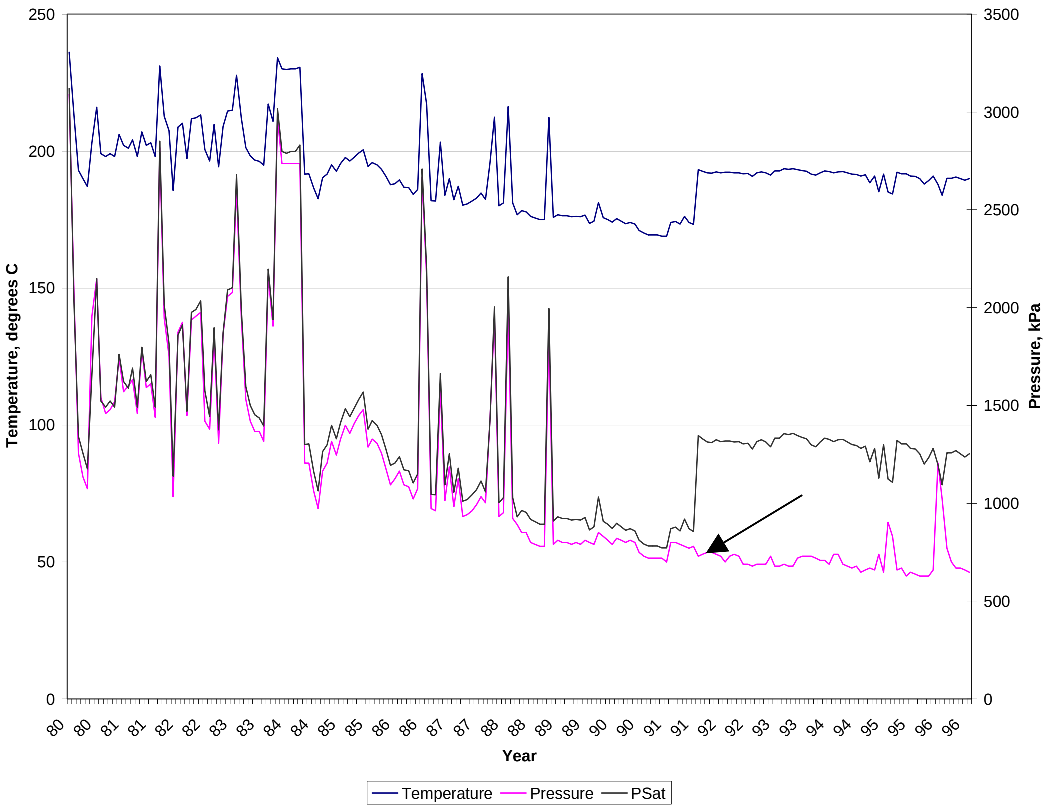

Figure 2-16: Saturated pressure values calculated from well temperature values and pressure values for the McKinley 1 well.

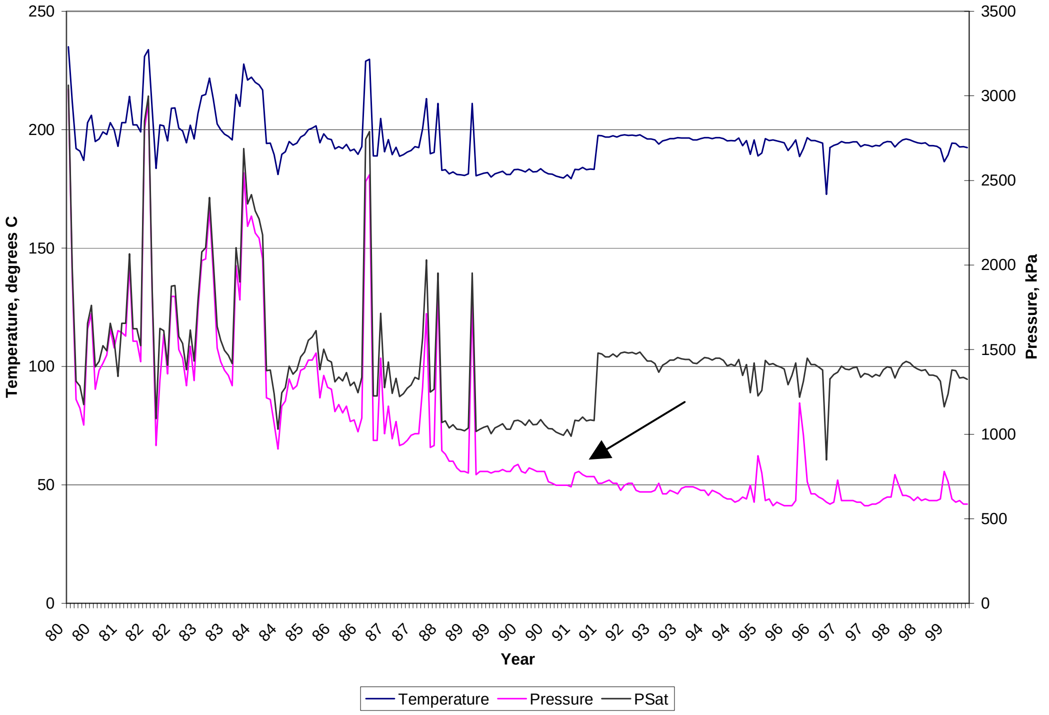

Figure 2-17: Saturated pressure values calculated from well temperature values and pressure values for the Thorne 1 well.

The Clausius-Clapeyron equation can be seen as a straight line by plotting ln(p) vs. 1/T. We can therefore extend this realization to the well data, assuming the elbow will not follow this straight line. Figure 2-18 shows this plot. We can therefore extend this realization to the well data, assuming the elbow will not follow this straight line. Figures 2-19 and 2-20 illustrate this premise, with the first part of the well data generally agreeing with the proposed linear relationship, and second part, the elbow, straying away from the line. The point which separates these two parts will be the dry-out temperature, T_d.

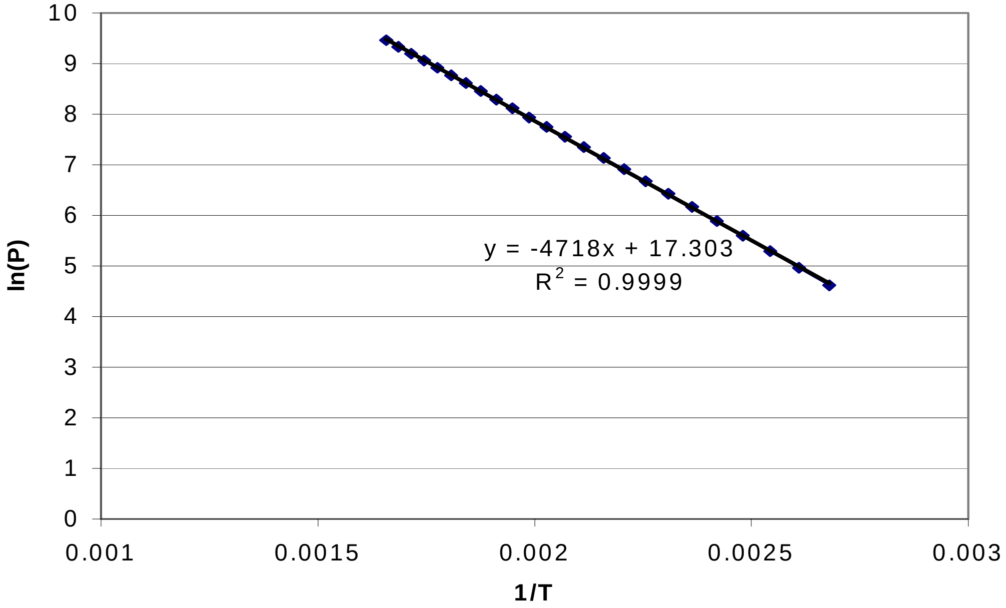

Figure 2-18: Plot of ln(p) vs. 1/T based on the Clausius-Clapeyron Equation.

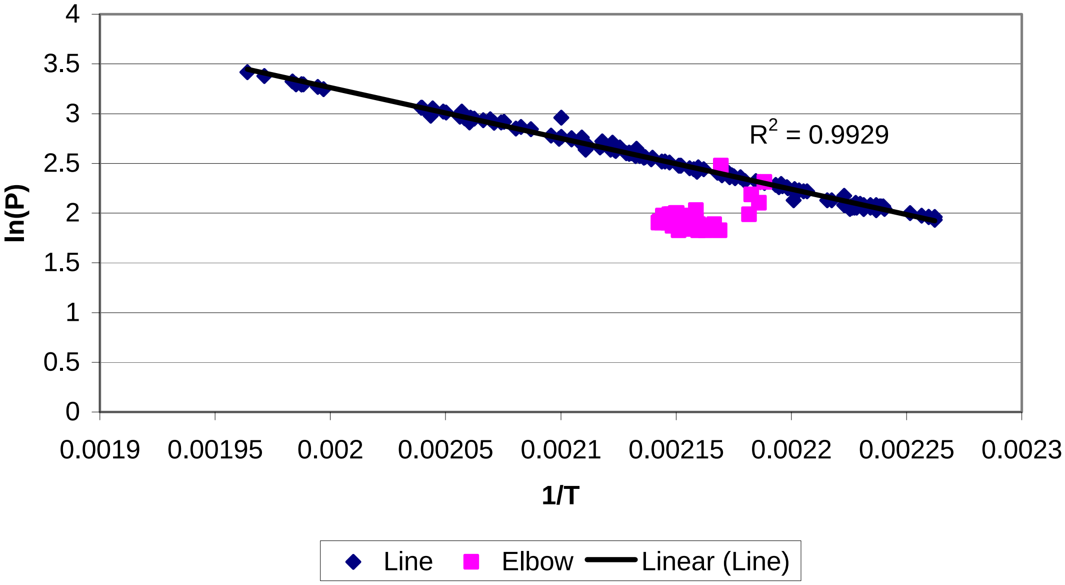

Figure 2-19: Plot of ln(p) vs. 1/T of the McKinley 1 pressure and temperature values to determine the dry-out temperature. The estimated T_d is 193.2 ºC.

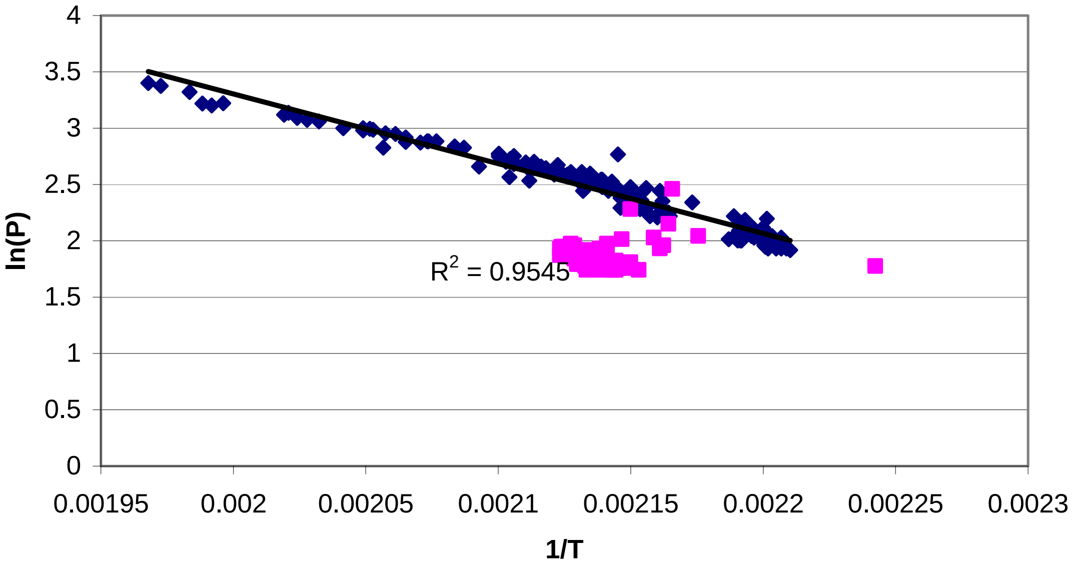

Figure 2-20: Plot of ln(p) vs. 1/T of the Thorne 1 pressure and temperature values to determine the dry-out temperature. The estimated T_d is 197.6 ºC.

Chapter 3

3. Estimated In-Situ Saturation Results

Before we use Equation 2-5 to calculate the in-situ saturation from the well production data for all the well in the database, we must know the various properties of the reservoir rock as well as the downhole initial and dry-out reservoir temperatures.

3.1. Evaluation of Temperature

The temperature data in the production database are derived from wellhead measurements. Since we need to know the downhole temperature rather than the wellhead temperature in order to calculate the saturation, a way to calculate the downhole temperature from the wellhead temperature is needed.

Horne (1988) describes a way to estimate the wellbore temperature and heat losses that facilitate the calculation of temperature profiles along a geothermal well. The equation for the evaluation of the temperature in a producing geothermal well is:

$$T = \left(T_{BH} - ay\right) + aA\left(1 - e^{-y/A}\right) + \left(T_O - T_{BH}\right)e^{-y/A} \tag{3-1}$$

where y is the distance upwards from the bottom of the well, T is the temperature needed at the given depth, T_O is the inflowing fluid temperature, T_{BH} is the downhole reservoir temperature, and a is the geothermal gradient. The parameter A is the diffusion depth which can be estimated by:

$$A(t) = \frac{Wcf(t)}{2\pi k} \tag{3-2}$$

where W is the mass flowrate, c is the thermal heat capacity of the fluid which is assumed to be constant, k is the thermal conductivity of the formation, and $f(t)$ is a dimensionless time function representing the transient heat transfer to the formation. For flowing time greater than 30 days, we can use an estimation of $f(t)$ by the equation:

$$f(t) = -\ln\frac{r}{2\sqrt{\alpha t}} - 0.29 \tag{3-3}$$

where α is the thermal diffusivity of the formation and r is the radius of the casing.

Since we are interested in calculating the bottomhole temperature from the given wellhead temperature, we set T in Equation 3-1 as T_{WH}, which is the wellhead temperature. Assuming the fluid temperature coming from the bottomhole is equal to T_{BH}, we get an equation that will be used for the evaluation of the bottomhole temperature in a producing well under single-phase flow:

$$T_{BH} = (T_{WH} + ay) - aA\left(1 - e^{-y/A}\right) \tag{3-4}$$

Thermal properties assumed for these calculations were derived from Walters and Combs (1989). Data on mass flowrate and flowing times were derived from the database. Depth of the well and the casing size were derived from well completion descriptions furnished by the companies that drilled the wells.

Figure 3-1 and Figure 3-2 plot the downhole temperatures and the wellhead temperatures, as well as the difference between these two temperatures, for McKinley 1 and Thorne 1, respectively.

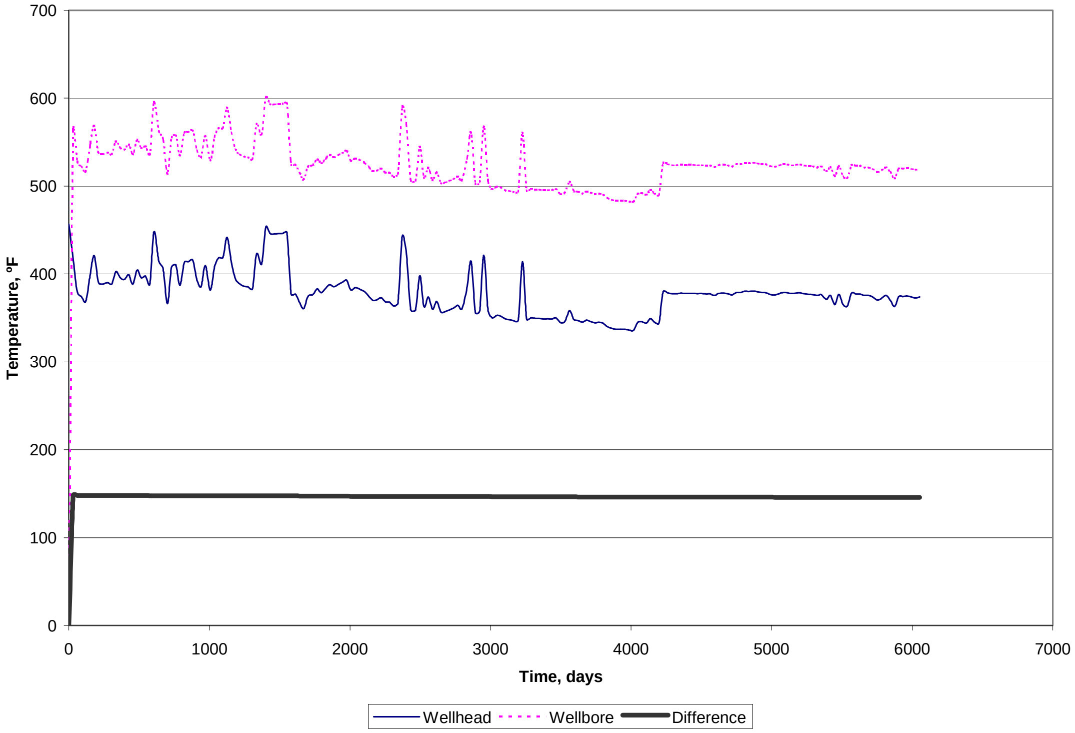

Figure 3-1: Wellhead and wellbore temperatures for McKinley 1 well.

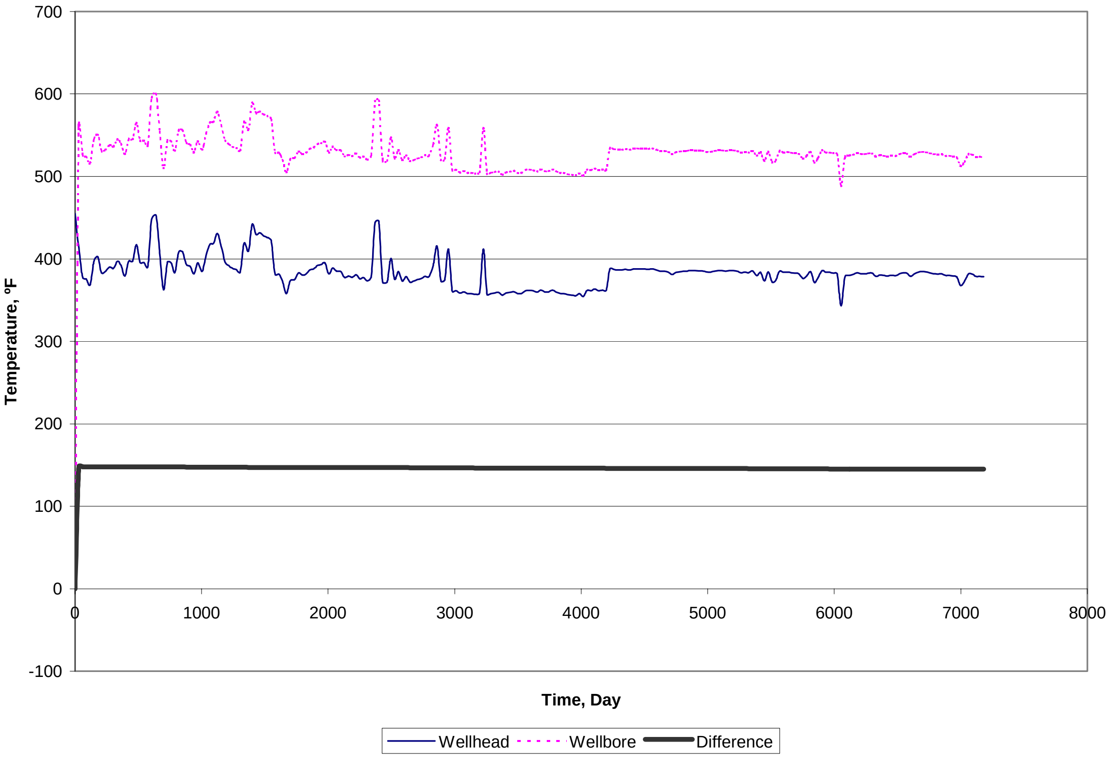

Figure 3-2: Wellhead and wellbore temperatures for Thorne 1 well.

The calculated difference between the wellbore and the wellhead temperature was between 146.2ºF and 147.99ºF for McKinley 1 and 146.1ºF and 147.99ºF for Thorne 1. This meant a 1.79 and 1.93 degree relative difference between the initial and dry-out temperatures for McKinley 1 and Thorne 1, respectively. The average difference in the initial and dry-out temperatures calculated for all the wells was 2.24 ºF, with a range of 0.267 to 7.11 ºF. This produced average percent increase in the estimated saturation values of about 12%, with a range of 0.11.

From the downhole temperature calculations for both wells, a range of values from 480 ºF to about 600 ºF were computed. This is consistent with the findings from Pham and Menzies (1993) that suggests a temperature of 470 ºF at saturation conditions, and temperatures greater than 500 ºF for depths greater than 1800 meters.

3.2. Evaluation of Other Properties

For the other reservoir rock properties, we searched existing literature to find values. The predominant reservoir rock is metagraywacke. Quoted values for the specific heat of this rock have ranged from 917 J/kg ºC (Barker et al. 1991), to values of 1000 J/kg ºC (Taylor, 1992 and Mossop et al. 1997). We assumed a specific heat of 960 J/kg ºC.

For rock density, Mossop et al. gave a Geysers rock density of 2700 kg/m^3. Estimates of Brown (1989) for graywacke densities range from 2660 kg/m^3 to 2770 kg/m^3. A rock density of 2700 kg/m^3 was be used for this study.

The rock porosity at the Geysers is fracture-related. Porosities of reservoir graywacke cores sampled by Gunderson (1992) ranged from a low of 0.6 percent to a high of 5.8 percent. Duba et al. (1992), used electrical properties of The Geysers as an indicator of porosity distribution, and the study derived a range of 0.973% to 6.54 %. Due to the presence of fractures, however, the actual bulk porosities are likely to be higher than the core samples used to estimate porosity of the rock matrix.

We investigated the effect of varying porosities on the calculation of in-situ saturation. Table 3-1 gives values of saturation ranges and average saturation values for various values of porosity and the other assumed reservoir rock properties.

Table 3-1: In-situ saturation values calculated from various porosity values.

	Porosity					
Saturation	**5.7 %**	**6 %**	**7 %**	**8 %**	**9 %**	**10 %**
Average	0.526	0.499	0.423	0.366	0.322	0.286
Low Value	0.207	0.196	0.167	0.144	0.127	0.113
High Value	0.999	0.946	0.803	0.695	0.598	0.544

The lowest assumed porosity of 5.7 % gives us saturation values ranging between 0.2 and close to 1. The highest assumed porosity, 10%, yielded a saturation value range of 0.11 to 0.54. Results from Willamson (1990) used history matching to infer an in-situ saturation of 82% for The Geysers. Pham et al. (1993) found that values of in-situ saturation ranging between 55% to 90% were necessary to obtain matches between simulated pressure values and field pressure values in their numerical model of the Geysers. In view of these findings, we used a porosity of 5.7% in our analysis.

3.3. Calculation of Saturation Values

Table 3-2 shows the calculated values of the saturations, as well as the values for T_o and T_d used to arrive at this result. We identified 177 wells in the database that show the presence of the dry-out point, therefore allowing the computation of the saturation values. The remaining 179 wells have data that are too sparse to observe any relationships.

Table 3-2: Calculated in-situ saturation values for 177 wells in The Geysers database.

Well Name	So	To	Td
Abel 1	0.505	196	178.3
Angeli 2	0.417	186.1	171.1
Angeli 3	0.407	186.1	170.6
Beigel 1	0.399	188.9	176.7
Beigel 2	0.535	195.6	175.6
Beigel 3	0.504	186.7	167.8
CA-1862 15A-21	0.999	208.3	172.8
CA-1862 15B-21	0.471	192.2	173.3
CA-1862 62D-29	0.370	193.7	178.9
CA-5636 23B-22	0.440	182.6	164.4
CA-5636 23G-22	0.483	187.6	167.9
CA-5636 23H-22	0.333	184.4	170.7
CA-5636 36C-22	0.386	181.9	165.9
CA-5636 68B-21	0.861	196.6	162.5
CA-5636 68D-21	0.931	197.9	161.2
CA-5636 74G-21	0.345	177.8	163.3
CA-5636 74H-21	0.331	177.4	163.5
CA-5636 87A-21	0.391	180.5	164.2
CA-5636 87B-21	0.553	182.3	159.4
CA-5636 87C-21	0.544	182.9	160.4
CA-5636 87D-21	0.874	197.4	162.9
CA-5636 87G-21	0.552	186.3	163.7
CA-5637 68-21	0.728	193.8	164.7
CA-5639 14A-27	0.401	201.12	186.7
CA-5639 15-28	0.580	191.1	169.4
CA-5639 15A-28	0.479	187.2	168.9
CA-5639 15C-28	0.311	181.7	170
CA-5639 15D-28	0.315	181.7	169.4
CA-5639 36-28	0.349	181.7	167.2
CA-5639 42-33	0.504	186.7	167.2
CA-5639 44-28	0.488	190	171.7
CA-5639 44A-28	0.505	187.2	168.3
CA-5639 44B-28	0.600	193.9	171.1
CA-5639 53-33	0.600	192.8	169.4
CA-5639 63-29	0.483	192.8	174.4
CA-5639 63A-29	0.766	197.8	168.9
CA-5639 63B-29	0.429	190.6	173.3
CA-5639 85-28	0.431	188.9	173.3
CA-5639 85A-28	0.398	187.8	172.8
CA-956A 56-34	0.626	194	172.7
CA-956A 56C-34	0.559	198.3	176.3
CA-956A 86-34	0.386	200.4	188.4
CA-958 37-34	0.644	197	175.2
CA-958 37A-34	0.553	196.5	181.7

Well Name	So	To	Td
CA-5634 21B-12	0.439	190.6	173.9
CA-5634 21D-12	0.443	190	173.3
CA-5634 32-12	0.379	186.1	171.7
CA-5634 32A-12	0.518	191.1	171.7
CA-5634 32B-12	0.424	187.8	172.2
CA-5634 32C-12	0.389	187.2	172.8
CA-5634 45B-12	0.425	187.8	171.1
CA-5634 52-11	0.672	200.6	176.1
CA-5635 117-19	0.570	192.2	170.6
CA-5635 123-19	0.381	183.3	169.4
CA-5635 94A-19	0.493	190.6	172.2
CA-5635 94B-19	0.702	197.2	171.1
CMHC 5	0.347	187.8	175.6
Coleman 1A-5	0.447	204.2	187.2
DX State 4596 22A	0.979	208.9	173.9
DX State 4596 23	0.570	193.3	172.8
DX State 4596 25	0.490	190.6	172.8
DX State 4596 27	0.475	187.8	172.8
DX State 4596 4	0.515	188.3	169.4
DX State 4596 40	0.455	191.1	174.4
DX State 4596 41	0.399	191.1	175
DX State 4596 42	0.654	197.8	174.4
DX State 4596 50	0.457	200.6	185
DX State 4596 56	0.432	186.4	171.1
DX State 4596 58	0.580	194.4	173.9
DX State 4596 59	0.586	195	173.3
DX State 4596 60	0.659	197.2	173.9
DX State 4596 62	0.299	183.3	171.7
DX State 4596 68	0.493	192.2	173.9
DX State 4596 69	0.642	197.2	174.4
DX State 4596 73	0.367	188.3	174.4
DX State 4596 74	0.351	185	172.2
DX State 4596 75	0.441	188.3	172.2
DX State 4596 76	0.666	198.9	173.3
DX State 4596 82	0.300	185.6	173.3
DX State 4596 85	0.525	193.3	172.8
Francisco 2-5	0.528	190.6	170
GDC 1	0.458	190	172.2
GDC 10	0.618	193.9	173.9
GDC 11	0.622	195.6	174.4
GDC 19	0.449	190	172.8
GDC 2	0.424	186.1	172.2
GDC 20-29	0.592	194.4	174.4
GDC 24	0.531	192.8	172.8

Well Name	So	To	Td
CA-958 37B-34	0.404	198.2	182.3
CA-958 37C-34	0.478	200.4	181.7
CA-958 56A-34	0.485	193	177.1
CA-958 56B-34	0.619	194.8	172.2
CA-958 86A-34	0.718	198.7	173.4
D & V 1	0.643	194.4	171.1
D & V 11	0.498	190	171.1
D & V 12	0.789	198.9	171.7
D & V 13	0.675	195.6	170.6
D & V 15	0.582	192.8	172.2
D & V 16	0.583	192.8	171.7
D & V 2	0.612	206.7	187.2
D & V 6	0.407	186.1	170
D & V A-2	0.994	202	168.8
D & V A-3	0.899	202	171.6
D & V A-4	0.840	199.9	169.1
GDC 23	0.439	185.6	169.4
GDC 29	0.462	190	173.9
LF State 4597 1	0.582	192.2	171.7
LF State 4597 10	0.749	195.6	168.3
LF State 4597 13	0.454	185	168.3
LF State 4597 37	0.641	193.3	168.9
LF State 4597 38	0.368	182.2	168.3
LF State 4597 42	0.406	187.8	172.2
LF State 4597 48	0.330	185	172.2
LF State 4597 49	0.328	185	172.2
McKinley 1	0.508	193	173.9
McKinley 10	0.612	203.7	182.5
McKinley 11	0.461	197.7	181
McKinley 12	0.493	192.4	175.2
McKinley 13	0.545	195.6	175.2
McKinley 15	0.750	206.6	177.9
McKinley 3	0.636	201	180.2
McKinley 4	0.623	204	183.6
McKinley 9	0.594	201.9	180.7
MLM 1	0.619	205	186
MLM 2	0.565	205	184.9
Modini 1	0.534	206.1	187.8
Modini 3	0.477	206.1	187.8
Modini 4	0.745	198.9	173.3
Thorne 1	0.446	199	183.4
Thorne 6	0.545	197	177.9
Tocher 3	0.573	197	175.6
CA-5634 21-12	0.468	191.7	174.4
CA-5634 21A-12	0.516	192.2	172.8

Well Name	So	To	Td
GDC 25	0.478	190	172.8
GDC 30	0.255	181.7	171.1
GDC 32A-13	0.668	192.8	168.3
GDC 66-12	0.706	194.4	170
GDC 7	0.529	189.4	171.7
GDC 8	0.207	193.3	185
GDC 85-12	0.583	185	166.1
GDC 86-12	0.762	195.6	169.4
GDC 9	0.489	190	173.9
Geyser Gun Club 6	0.492	193.3	175.6
Geyser Gun Club 8	0.396	190.6	176.1
Happy Jack 11	0.437	185.6	170
LF State 4597 12	0.442	185	169.4
LF State 4597 14	0.464	185	168.9
LF State 4597 18	0.543	192.8	172.8
LF State 4597 27	0.413	187.2	172.2
LF State 4597 28	0.496	190.6	172.2
LF State 4597 29	0.433	188.3	172.2
LF State 4597 31	0.425	185	169.4
LF State 4597 34	0.534	192.2	172.8
LF State 4597 36	0.466	189.4	172.2
LF State 4597 4	0.644	190.6	168.3
LF State 4597 5	0.735	196.7	172.8
Ottoboni St 4596 13	0.454	190.6	173.9
Ottoboni St 4596 14	0.328	185.6	174.4
Ottoboni St 4596 16	0.366	185	172.2
Ottoboni St 4596 18	0.445	187.2	171.2
Ottoboni St 4596 23	0.614	190.6	171.1
Ottoboni St 4596 24	0.568	186.7	170
Ottoboni St 4596 29	0.346	187.2	173.9
Sulphur Bank 10	0.487	177.8	159.4
Sulphur Bank 11	0.756	186.1	162.2
Sulphur Bank 14	0.539	177.2	160.6
Sulphur Bank 17	0.781	188.9	158.4
Sulphur Bank 20	0.517	187.2	166.1
Sulphur Bank 21	0.423	182.2	167.2
Sulphur Bank 22	0.504	185	166.7
Sulphur Bank 23	0.635	192.2	166.7
Sulphur Bank 24	0.727	197.8	171.1
Sulphur Bank 26	0.426	187.2	171.7
Sulphur Bank 27	0.534	190.6	171.7
Sulphur Bank 28	0.436	190.6	174.4
Sulphur Bank 30	0.522	187.2	167.8
Sulphur Bank 31	0.406	190	174.4
Sulphur Bank 8	0.639	185.6	159.4

To understand the spatial trends of saturation values in the Cartesian plane, we mapped out different types of wells we classified. Figure 3-3 shows an aerial view of a contour plot made by the saturation values. The two boxes located in the upper-left region of the plot, and the lower-left region of the plot correspond to the Northwest (NW) and Southeast (SE) zones, respectively. We can see that in the SE location, we have mostly blue colors, signifying a higher average saturation values (0.55). In the NW location, we see orange and yellow values, indicating that there is a concentration of lower average saturation value in this zone (0.5).

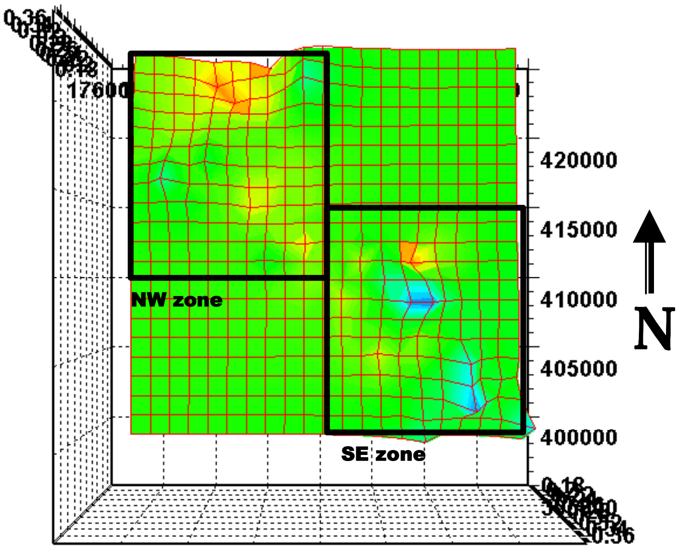

Figure 3-3: Aerial view contour plot of the saturation values on the Cartesian plane of the 177 superheated Geyser wells.

3.4. Other Wells

We identified wells that do not have a discernable change in trend, and therefore infer that these wells have not reached superheat. Figure 3-4 shows an example of such a well, and as we can see the relationship between the pressure and temperature is direct all throughout the history. We identified 147 wells that exhibit this trend.

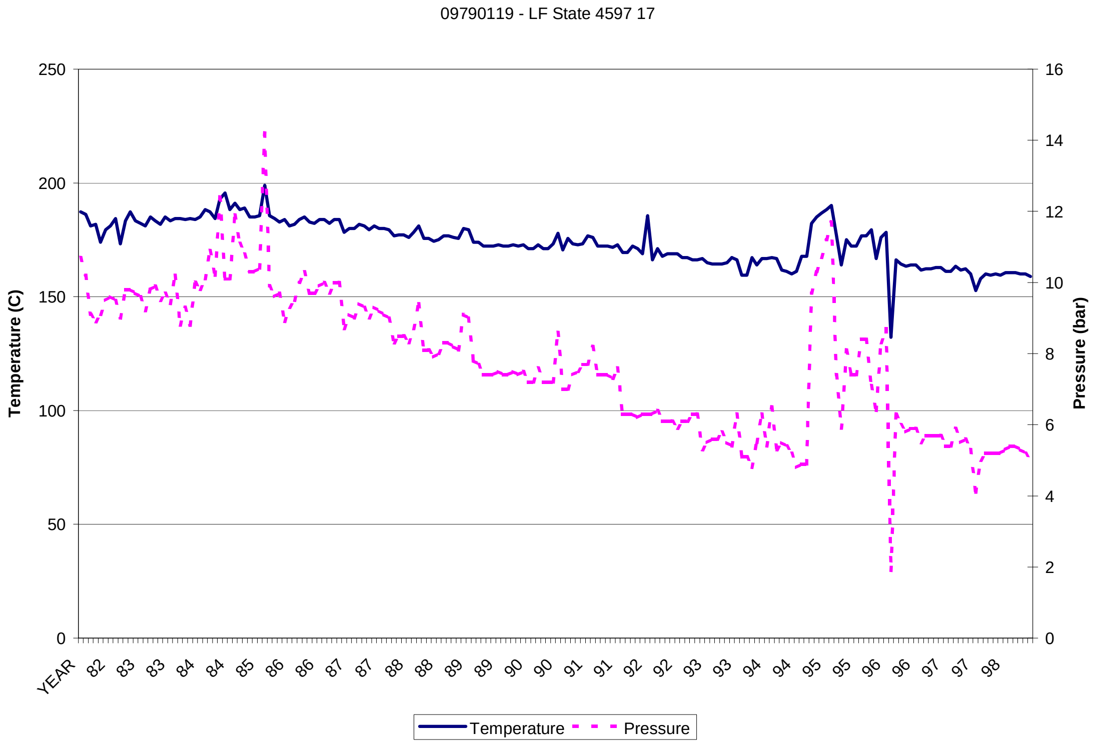

Figure 3-4: Temperature and pressure values history for a well with no dry-out point.

The remaining 179 wells have data that are too sparse to observe any relationships. An example of such a well is shown in Figure 3-5. We also identified 25 injection wells from the database.

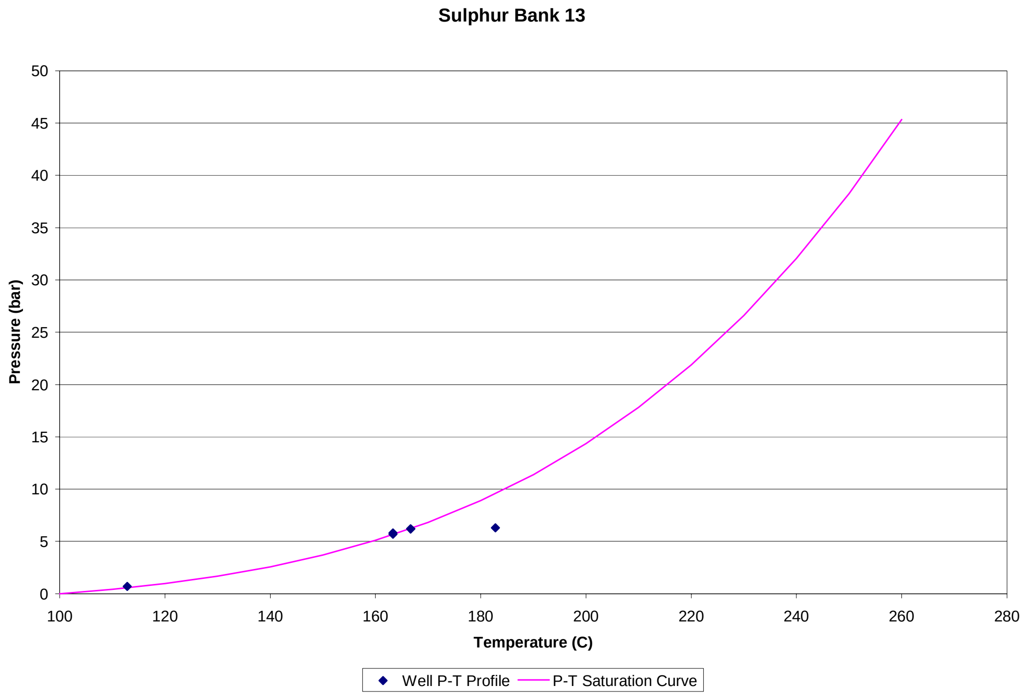

Figure 3-5: Pressure-temperature profile of a well with sparse data.

Figure 3-6 shows the plot of wells that have not yet reached superheat, which we call "saturated" wells, on the Cartesian plane. The NW zone has 64% of all the saturated wells, indicating that there is a higher number of saturated wells in the NW zone than in the SE zone.

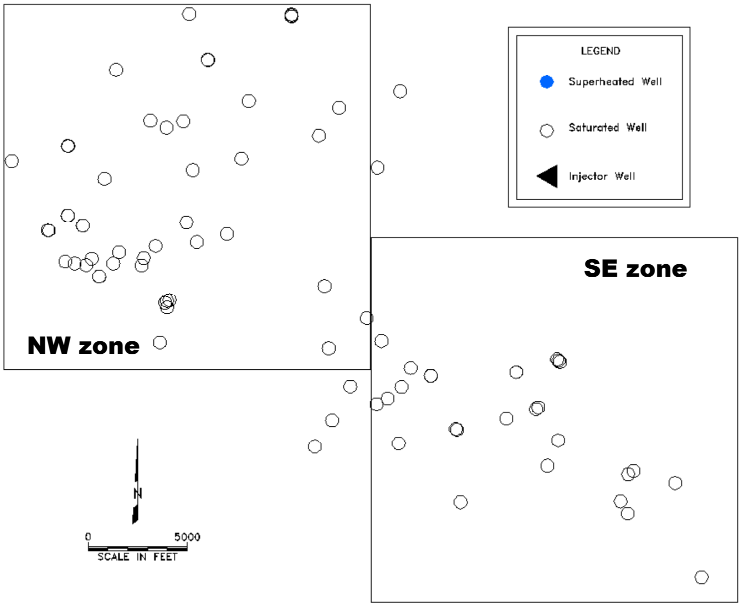
LEGEND
Superheated Well
Saturated Well
Injector Well
SE zone
NW zone
N
0
5000
SCALE IN FEET

Figure 3-6: : Locations of the saturated wells.

Chapter 4

4. Direct Measurement of the In-Situ Saturation

As a second component of this study, we also made direct measurements of the irreducible water saturation in cores from The Geysers, in order to make direct comparisons with the inferred water saturations estimated as described in Chapter 4. The direct measurements used cores cut from a Geysers well, with an X-ray CT method.

A problem of using the X-ray CT method to measure fluid saturations along the longitudinal direction in the core samples was solved during this study. Significant X-ray beam-hardening effects occur when the core sample is scanned in the longitudinal direction. Installation of core systems in water jackets or in sand packs has been a frequently used method to reduce beam-hardening effects. Such a method may not be convenient and may not work in some cases. A new approach was developed to measure fluid saturations in the longitudinal direction. The main idea is to scan core samples at a specific angle deviated from the longitudinal direction to avoid the edges of the core and the coreholder. The shape of CT images obtained in such a way is elliptical. The fluid saturation in the longitudinal direction can then be inferred according to the angle of deviation.

4.1. Method

The water saturation in the core was measured by using an X-ray CT method. Water saturation is calculated as follows:

$$S_w = \frac{CT_{\exp}(T) - CT_{dry}(T)}{CT_{wet}(T) - CT_{dry}(T)} \qquad \textbf{(4-1)}$$

where $CT_{wet}(T)$, $CT_{dry}(T)$ are CT numbers of the core sample when it is fully saturated by water and steam respectively; $CT_{exp}(T)$ is the CT number of the rock when it is partially saturated by steam, all at the same temperature T.

Porosity of the core measured by using an X-ray CT technique is computed using the following expression:

$$\phi = \frac{CT_{wet}(T) - CT_{dry}(T)}{CT_{water}(T) - CT_{air}(T)} \qquad \textbf{(4-2)}$$

where CT_{water} and CT_{air} are the CT numbers of water and air respectively.

4.2. Experiments

Rock and Fluids. The liquid phase used in this study was distilled water; the specific gravity and viscosity were 1.0 and 1.0 cp at 20^oC. Steam was the gas phase; the surface tension of water/steam at 20^oC was 72.75 dynes/cm, which was assumed to be the same as the surface tension of water/air. The values of the surface tension at high temperatures were calculated from the steam property software developed by Techware Engineering Applications, Inc.

The Geysers rock sample from a depth of about 1410.1m was obtained from the Energy and Geoscience Institute; its porosity measured using an X-ray CT technique was about 3.1 %. The matrix permeability of the rock sample has not been measured yet because of the fractures in epoxy between the core sample and the coreholder. The permeability of a nearby sample measured by nitrogen injection was about 0.56 md (after calibration of gas slip effect), which is probably attributed mainly to the fracture permeability. The length and diameter of this rock sample were 8.89 cm and 8.56 cm.

X-ray CT Scanner. Distribution of water saturation in the core sample was measured using a Picker^{TM} Synerview X-ray CT scanner (Model 1200 SX) with 1200 fixed detectors. The voxel dimension was 0.5 mm by 0.5 mm by 5 mm, the tube current used was 50 mA, and the energy level of the radiation was 140 keV. The acquisition time of one image was about 3 seconds while the processing time was around 40 seconds.

Experimental Apparatus. An apparatus was developed to measure in-situ water saturation in The Geysers rock at high temperature. A schematic of the apparatus is shown in Figure 4-1.

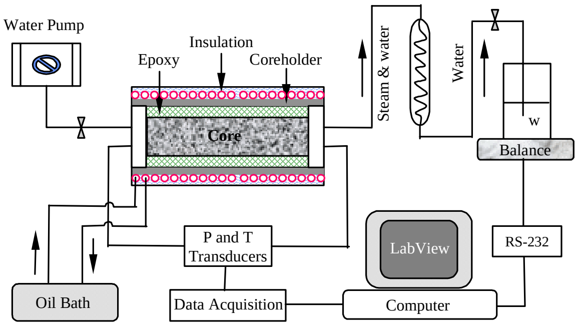

Figure 4-1: Schematic of the apparatus used to measure in-situ water saturation.

The apparatus was composed of core and coreholder system, temperature controlling system, pump system (water delivering pump and vacuum pump), production metering system (using a balance), pressure transducers, thermal couples, and data acquisition system. The vacuum pump is not shown in Figure 4-1. The data acquisition software used was LabView 6.0 by National Instrument Company.

The vacuum pump (Welch Technology, Inc., Model 8915) was used to remove the air in the core sample in order to generate the steam-water environments. A cold trap with dry ice was employed to protect the steam from entering the vacuum pump to extend its life and reduce the frequency of replacing the pump oil.

Water was delivered by the water pump (Dynamax, Model SD-200), manufactured by RAININ Instrument Co., and the amount was measured by the scale (Mettler, Model PE 1600) with an accuracy of 0.01g and a range from 0 to 1600g. The water injected into or produced from the core sample was recorded in time by the balance and the real-time data were measured by a computer through an RS-232 interface.

The temperature in the core was controlled automatically using an oil bath (manufactured by VWR, Model 9401) through an external aluminum coil mounted closely on the outside of the coreholder. Aluminum was used to be transparent to the X-rays. In order to obtain a uniform temperature distribution along the core, the aluminum coil was designed as shown in Figure 4-2. The oil-in tubing was arranged close to the oil-out tubing. There are two ways to realize this arrangements. One way is to make the aluminum tubing a U-shape first. One end of the U-shape tubing is the oil inlet and another end is the oil outlet. The oil-in and oil-out tubes are put together and then wrapped on the coreholder. Another way is to wrap the oil-in (or oil-out) tube on the coreholder first, from the inlet to the outlet of the coreholder. A U-turn can be made on the end surface of the coreholder and then the tube wrapped back from the outlet to the inlet, as shown in Figure 4-2. We chose the latter technique. In such a tubing arrangement, the cooling of the oil temperature in the oil-out tubing could be compensated almost instantly by the oil with high temperature in the oil-in tubing.

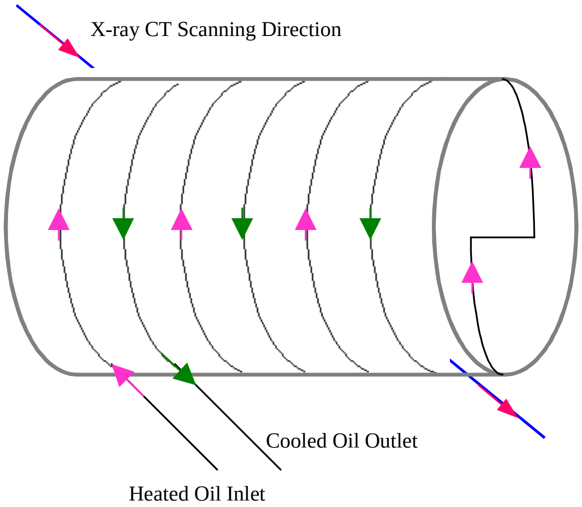

Figure 4-2: Schematic of the aluminum coil used to control the temperature in the core.

Temperatures at both the inlet and the outlet of the core were measured during the experiment. We found that temperatures at the inlet were equal to those at the outlet in most cases.

The procedure to make the core system is described briefly as follows. The core was machined and inserted into an aluminum cylinder filled with high temperature epoxy. The core and coreholder system with epoxy was then cured at a temperature of about 160°C. A specific length of the top and the bottom sections of the coreholder with the core sample inside were cut off to remove the epoxy on the top and the bottom surfaces of the core sample. Two end plates with O-rings were then installed to seal the core and the coreholder system using eight screws.

Small cracks in the epoxy between the outside surface of the core sample and the inner side of the coreholder were found after the epoxy was cured. This might be caused by the different heat expansion coefficients among aluminum, rock, and epoxy. Note that we could still measure in-situ water saturation in the core sample by using an X-ray CT technique even with cracks in the epoxy. However we could not measure the permeability of the core in this case.

A picture of the core and the core holder system prior to wrapping insulation material is shown in Figure 4-3. The black rubber tubes were the insulation material for the oil-in and oil-out tubing connected to the oil bath. The gantry of the X-ray CT scanner is visible right hand side.

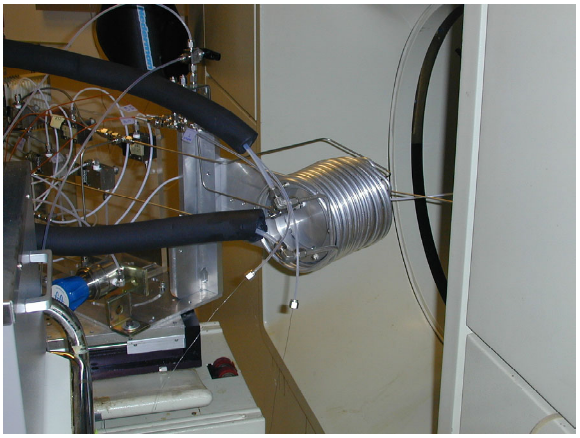

Figure 4-3: Picture of the core and core holder system prior to wrapping insulation material.

A picture of the back view of the apparatus after wrapping insulation material over the coreholder is shown in Figure 3-4.

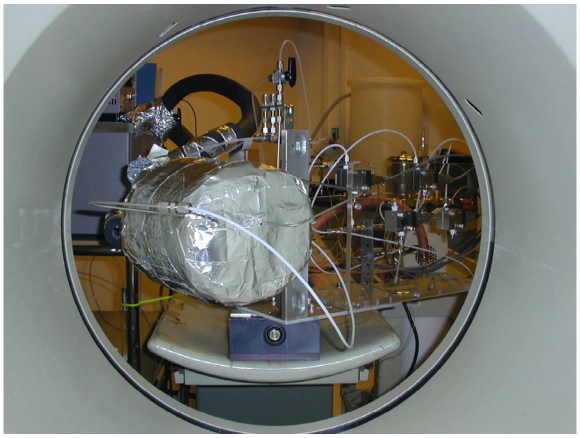

Figure 4-4: Picture of back view of the apparatus.

Figure 4-5 shows a picture of the whole apparatus. A web camera (installed on the tripod in Figure 4-5) was used to monitor the status of the experiments. Because of the long test time, some devices may fail to function. Using the web camera, we could monitor the laboratory whenever we wanted to and from wherever we were, once an internet access is available. We found that it was very convenient and helpful to have the web camera installed.

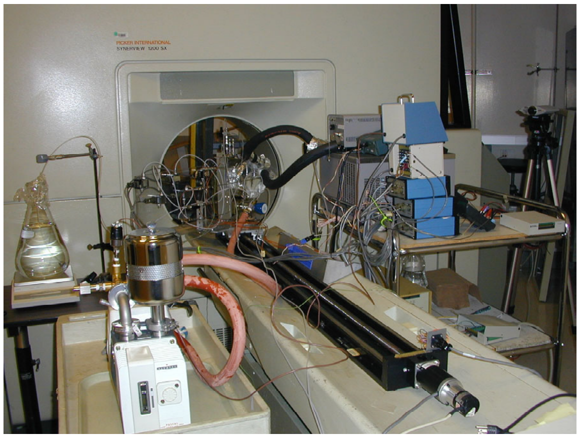

Figure 4-5: Picture of the whole apparatus used to measure in-situ water saturation.

Procedure. The apparatus was installed according to the schematic shown in Figure 4-1. The core sample assembled in the coreholder was dried by heating to a temperature of about 120°C while pulling a vacuum for approximate 48 hours. The core was scanned from time to time to monitor the variation of water saturation in the rock until the core was dry. The CT value of the dry core (CT_{dry}) was obtained. The core was then saturated with water by pulling a vacuum after the core and the coreholder system was cooled to room temperature. After the saturation of water, the core sample was pressurized to about 75 psi and kept at this pressure for about five days to let the core sample saturate with water completely. The core sample was flooded by water injection following that. The core sample was scanned after saturating with water. The CT value of the wet core

(CT_{wet}) was obtained. Porosity of the rock was then calculated using Eq. 1 with these CT values.

The temperature of the core saturated with water was increased from room temperature to about 120°C step by step using the oil bath through the aluminum coil wrapped outside the coreholder. The pore pressure in the core sample was kept about 50 psi, far above the saturation pressure, 14.4 psig, at a temperature of 120°C. The core was scanned from time to time to obseve the effect of temperature on CT values of the core sample.

Pressure in the core sample was decreased gradually to the atmospheric pressure to investigate the dependence of in-situ fluid saturation in the core sample on temperature and pressure. The production was recorded with time.

4.3. Results

Fluid saturation in the core sample was measured using a modified X-ray CT technique. As stated previously, scanning the core in a direction at an angle (see Figure 4-2) deviated from the axis of the core may reduce X-ray beam-hardening effect caused by sharp edges of rectangular objects. By inclining the core, the cross-section is made elliptical and we were able to obtain the distribution of the CT values from the inlet to the outlet of the core sample through just one scanning.

Figure 4-6 shows the CT image obtained by scanning the core sample in the regular longitudinal direction before installed in the coreholder. Significant beam-hardening effect (dark X-shape) can be seen in the diagonal directions on the rectangular area. The core sample was positioned vertically. The CT images obtained by scanning the core sample in the direction perpendicular to the longitudinal axis demonstrated that the image did not have the X-shape distribution of CT values (see Figure 4-6). The X-shape beam-hardening effect is often observed if the scanning direction is in the longitudinal direction. Other types of beam-hardening effect may also be observed. All the artifacts caused by the X-ray beam-hardening effect reduce the accuracy of calculating fluid saturations significantly. It is important to obtain CT images without artifacts caused by X-ray beam-hardening effect.

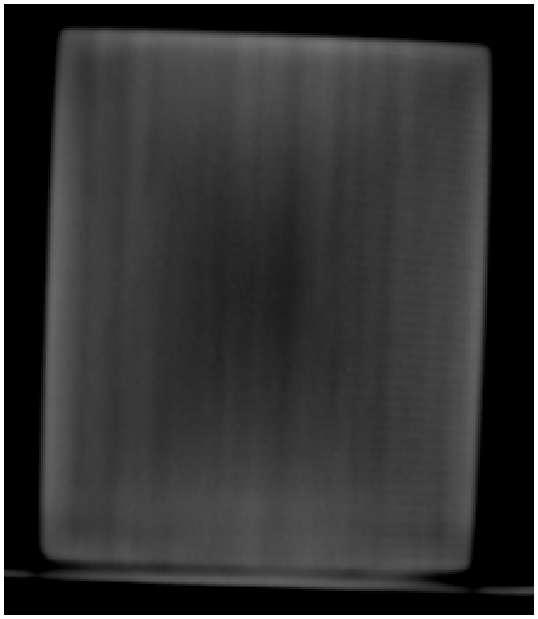

Figure 4-6: CT image obtained by scanning the core sample in the longitudinal direction.

The CT image obtained by scanning the core sample at an angle to the longitudinal direction is shown in Figure 4-7. The image shape presented to the scanner becomes elliptical, and the X-ray beam-hardening effects are avoided.

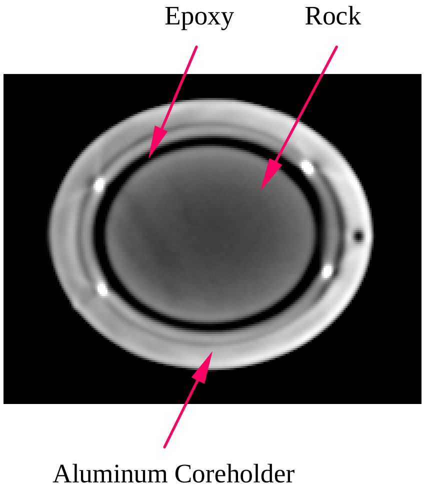

Figure 4-7: CT image obtained by scanning the core sample inclined to the longitudinal direction.

One can see from Figure 4-7 that the beam-hardening effect was reduced significantly by using the modified scanning technique. Note that the CT image in Figure 4-7 has different size from that in Figure 4-6. This is because the scanning size (diameter of scanning area) was changed for the image in Figure 4-7 to fit the position requirements for the installation of the coreholder.

Li and Horne (2001) observed a significant effect of temperature on the CT value of Berea sandstone saturated with water. However the effect of temperature on CT value of The Geysers rock saturated with water was found to be almost negligible, as shown in Figure 4-8. The reason may be because of the small porosity of The Geysers rock. The temperature varied from room temperature to about 120^{o}C.

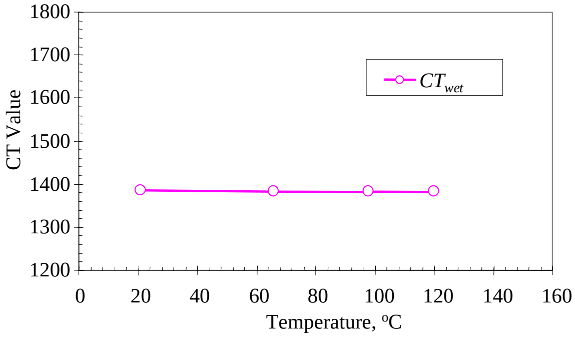

Figure 4-8: Effect of temperature on the CT value of the core sample saturated with water.

In the blowdown experiment, the CT value of The Geysers rock saturated with water at a temperature of about 120^{o}C decreased with decrease in the pore pressure, as shown in Figure 4-9.

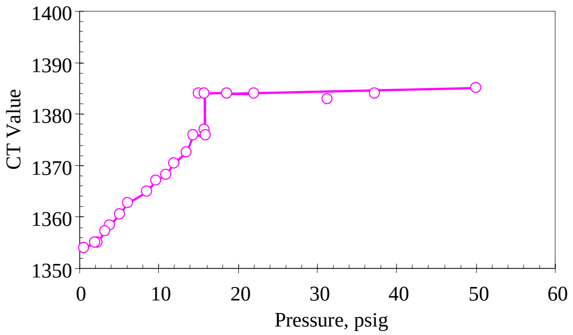

Figure 4-9: Pressure and CT value history of The Geysers rock saturated with **water.**

The values of the in-situ water saturation were calculated using Eq. 1 with the CT data shown in Figure 4-9. The results are plotted in Figure 4-10. The variation of the in-situ water saturation with pressure is similar as the variation of the CT value (CT_{wet}) with pressure (see Figure 4-9).

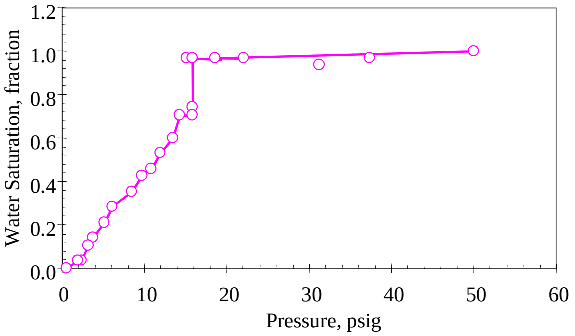

Figure 4-10: Variation of in-situ water saturation in The Geysers rock with pressure at a temperature of 120°C.

One can see from Figure 4-10 that there is a sharp drop in the water saturation at a pressure close to the saturation pressure (14.4 psig) at 120°C. The corresponding in-situ water saturation is about 70%. This value should represent the immobile water saturation in the core sample. Note that this value obtained in The Geysers rock is much greater than those measured in Berea sandstone reported by Li *et al*. (2001) and Horne *et al*. (2000). Li *et al*. (2001), who conducted similar experiments in Berea sandstone, also observed a sharp drop in water saturation at a pressure close to the saturation pressure. The corresponding in-situ water saturation in Berea sandstone was about 38%. Note that water saturation was not measured using an X-ray CT technique in that study. Instead, a weighing method was used. So the water saturation measured by Li *et al*. (2001) represented the average value in the whole core.

Horne *et al*. (2000) measured steam-water relative permeability in Berea sandstone using an X-ray CT technique. The measured value of the immobile water saturation in the Berea sandstone sample with a permeability of 1200 md was about 27%. This value is much smaller than the value of 70% in The Geysers rock, as stated previously. The reason may be because of the extremely low permeability of The Geysers rock.

Estimates of the initial in-situ water saturation inferred using field data in Chapter 3 ranged from 33% to 87%. Note that these are not inconsistent values, since there is no constraint that the initial water saturation be equal to the immobile water saturation.

Reyes and Horne (2002) reported that vapor-dominated geothermal reservoir under exploitation can be locally depleted of water to form a dry or superheated zone. One can also observe such a phenomenon in the experiments conducted in this study, as shown in Figure 4-10. After the sharp drop, the in-situ water saturation in The Geysers rock decreased to zero gradually (see Figure 4-10) as the pore pressure decreased to atmospheric pressure. Compared to Berea sandstone, the decrease in the in-situ water saturation in The Geysers rock is slower.

4.4. Discussion

The experimental results reported in this article are preliminary because of the very limited number of experiments conducted. It took a long time for almost every step and procedure, even for saturating the core with water. One day after saturation with water by pulling a vacuum, the inlet and the outlet of the core system were closed. Following that, the pressure in the core sample was monitored continuously. It was found that the pore pressure in The Geysers rock went below the atmospheric pressure. We speculated that the reason might be because of the extremely low permeability of The Geysers rock. It may take a very long time for water to get into the rock with low permeability just by pulling a vacuum.

In order to saturate the core sample with water completely, water was injected continuously. The inlet and the outlet were closed after a specific period of water injection to see if the pore pressures were going down. Water injection did not stop until the pore pressure could stabilize after the inlet and the outlet ends were closed. Then the core sample was pressurized to about 50 psig to further saturate with water.

The in-situ water saturation in the Geysers rock was decreased from 100% to zero by decreasing the pressure in the core sample. It also took a long time to stabilize the pore pressure in the matrix of the core sample after drawing down the pressure in fractures by opening the outlet valve.

Chapter 5

5. Effect of Reinjection

To investigate the possible effect of an increase of the calculated saturation values due to reinjection, we plotted the locations of the injection wells in the Cartesian plane. Figure 6-1 shows the plot, and we can say that these wells are evenly distributed throughout the field.

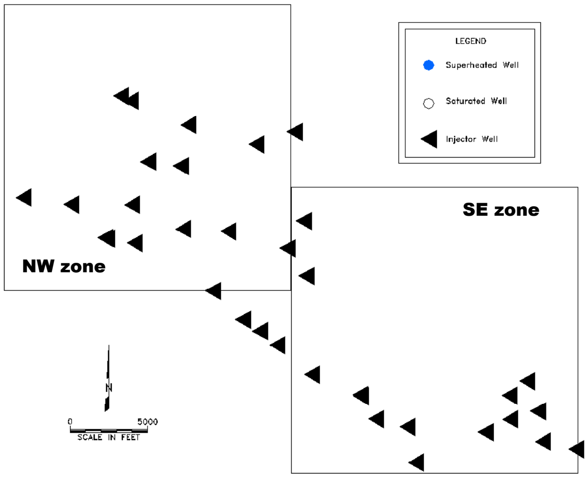

Figure 5-1: Locations of the injection wells.

5.1. Simulation of Reinjection

We analyzed the trends presented so far further by simulating the influence of reinjection in the vicinity of a producing well using TOUGH2. In the simulation, we injected water at constant flowrate and 20ºC temperature to the grid cell farthest from the center of the radial model used in previous simulations. We used a value of 0.3 for the in-situ water saturation and we investigated whether reinjection affects the estimates of this value from the zero-dimensional model. The temperature and pressure profiles for this simulation are plotted in Figure 5-2.

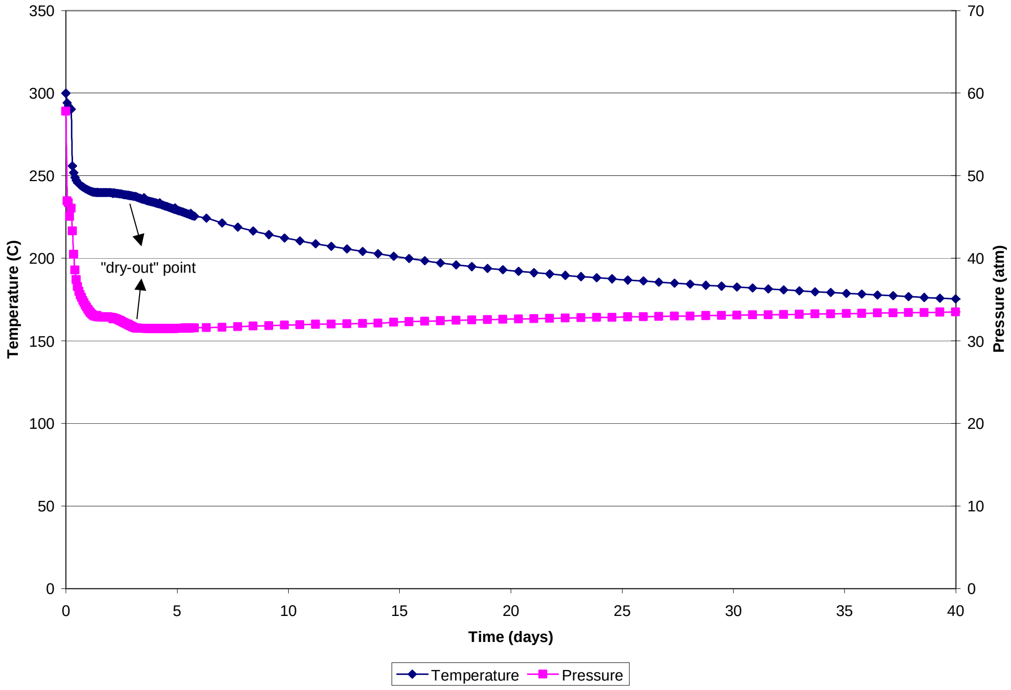

Figure 5-2: Pressure-temperature history showing the dry-out point for a simulation run showing reinjection.

In Figure 5-2 we have identified the zones of direct and inverse relationships, therefore we can use this to identify the T_o and T_d values to calculate the in-situ water saturation from the zero-dimensional model. If we calculate the in-situ saturation, the original saturation of 0.3 appears to increase to 0.36, indicating that indeed reinjection increases estimated value of the in-situ water saturation in the well.

We might therefore attribute the high saturation values found in the SE zone of the Geysers to be a result of reinjection. It is known that in this zone, we have the presence of an enhanced water supply (from the Lake County waste water project), therefore this, coupled with a lowering of pressure in the zone, contributes to the high apparent saturation values.

5.2. Effect of Reinjection Location

We further investigated the effect of reinjection by varying the flowrate of reinjection and the location of reinjection. We fixed an in-situ saturation as 0.3 in the simulator, with reservoir properties shown in Table 2-1. At the center we put a production well with a production index of 1 x 10^{-13} operating against a downhole pressure of 1378.6 kPa.

We varied the location of the reinjection by placing reinjection wells in the locations shown in Figure 4-3. The names A31, A51 and A81 correspond to the gridblock number where reinjection occurs The reinjection flowrate was fixed to be 20% of the average production flowrate from the previous simulation. Table 5-1 summarizes the effect of location on the saturation value of the reservoir.

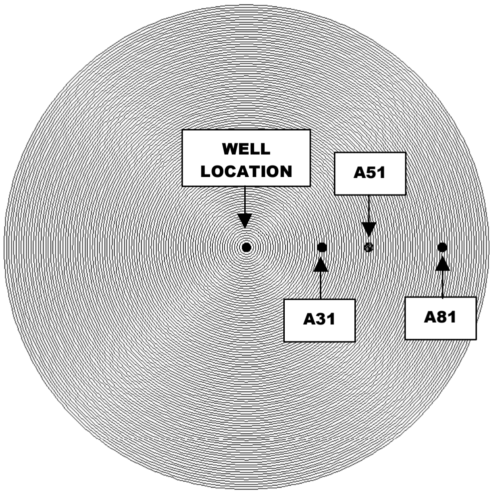

Figure 5-3: Production well and reinjection well locations in the simulation model.

Table 5-1: Effect of location of reinjection well to the in-situ water saturation value.

Gridblock	**S_o**	**T_o**	**T_d**
A31	0.479	300	280
A51	0.455	300	281
A81	0.335	300	286

We can see from the Table 5-1 that A31, the reinjection well nearest to the production well, has the highest apparent saturation value (0.48). The saturation value from the farthest reinjection well (A81), provided us a value of 0.33. We can see from this that the well location affects the calculated saturation value of the well.

5.3. Effect of Reinjection Flowrate

We investigated the effect of flowrate by assuming higher and lower flowrates from the original flowrate of 16% of the original production well case. We placed the wells in block A51. The results are summarized in Table 5-2.

Table 5-2: Effect of flowrate of the reinjection well to the in-situ water saturation value.

Flowrate	S_o	T_o	T_d
0.3 kg/s (4 %)	0.431	300	282
0.8 kg/s (16 %)	0.455	300	281
2 kg/s (40 %)	0.479	300	280

We can see from the Table 5-2 that a higher flowrate means a higher inferred saturation value, and reinjection at 4 % of the production flowrate yields the lowest inferred saturation value.

6. Conclusions

1. Vapor-dominated geothermal reservoirs under exploitation can be depleted locally of water to form a dry or superheated zone.

2. Well performance data history can be used to infer in-situ water saturation.

3. A geothermal reservoir can be said to have dried-out when its pressure-temperature profile deviates from the steam saturation curve.

4. Zero-dimensional models can be used to calculate the in-situ water saturation after identifying the initial reservoir temperature and the dry-out temperature.

5. Based on our estimates, prior to exploitation The Geysers wells had an average in-situ water saturation of 0.55 in the Southwest zone. The wells in the Northwest zone had an average value of 0.5. These values are consistent with inferences made by earlier authors using numerical models of the field.

6. The immobile in-situ water saturation in The Geysers rock measured using the experimental technique developed in this study was about 70%. This value represents the saturation of the rock matrix itself, since the core sample did not include large fractures such as may be present in the reservoir itself.

7. The experimental measurement is consistent with the estimates of the water saturation based on field data as well with inference from reservoir simulation models published by earlier authors.

8. An increase in apparent in-situ saturation is attributable to reinjection of water, and may also be affected by the location and rate of reinjection. This influence may explain the apparently higher in-situ water saturation in the Southwest zone.

Nomenclature

a = geothermal gradient
C = specific heat capacity
c = compressibility
h = enthalpy
k = permeability
k = thermal conductivity
p = pressure
r = radius
R = ideal gas constant
R = correlation value
s = saturation
T = temperature
t = time
y = depth
u = velocity
V = volume
α = thermal diffusivity
ϕ = porosity
μ = dynamic viscosity
ρ = density
ν = kinematic viscosity

BH = bottomhole
d = dry-out conditions
g = gas
o = initial conditions
r = rock
s = steam

vap = vapor
w = water
WH = wellhead

References

Barker, B., Gulati, M., and Riedel, K.L.: “Geysers Reservoir Performance,” *Geothermal Resources Council*, Monograph on the Geysers Geothermal Field, Special Report No. 17, pp 167 – 177. 1991.

Barker, B., and Pingol, A.: “Geyser Reservoir Performance – An Update,” *Proceedings*, Twenty Second Workshop on Geothermal Reservoir Engineering, Stanford University, California, Stanford, January 27-29, 1997; SGP-TR-155.

Belen, R.P., Jr.. and Horne, R.N.: "Inferring In-Situ and Immobile Water Saturations from Field Measurements", *Geothermal Resources Council*, Trans. **24** (2000).

Bowen, R.: “*Geothermal Resources*,” 2nd Edition, Elsevier Science Publishing Co., Inc, New York, 1989.

Brown, J.M.: “Bedrock Geotechnical Properties Affecting groundwater Movement in the U.S. Coast Guard Reservation, Kodiak, Alaska.” *Alaska Division of Geological and Geophysical Surveys*, Alaska Pacific University. 1989.

Grant, M., Donaldson, I., and Bixley, P.: “*Geothermal Reservoir Engineering*,” Academic Press, Inc., New York, 1982.

Gunderson, R.P.: “Porosity of Reservoir Graywacke at the Geysers,” *Geothermal Resources Council*, Monograph on The Geysers Geothermal Field, Special Report No. 17, pp. 89 – 96. 1992.

Horne, R.N.: “Geothermal Energy Assessment”, in *Geothermal Reservoir Engineering*, editor E. Okandan, Reidel. pp. 6-1 – 6-26. 1988.

Horne, R.N., Satik, C., Mahiya, G., Li, K., Ambusso, W., Tovar, R., Wang, C., and Nassori, H.: “Steam-Water Relative Permeability,” presented at World Geothermal Congress, Kyushu-Tohoku, Japan, May 28-June 10, 2000; *GRC* Trans. **24** (2000).

Li, K., Nassori, H., and Horne, R.N.: “Experimental Study of Water Injection into Geothermal Reservoirs,” proceedings of the GRC 2001 annual meeting, August 26-29, 2001, San Diego, USA; *GRC* Trans. V. **25** (2001).

Li, K. and Horne, R.N.: “An Experimental and Theoretical Study of Steam-Water Capillary Pressure,” *SPEREE* (December 2001), p.477-482.

Mossop, A. and Segall, P.: “Subsidence at the Geysers Geothermal Field, N. California from a Comparison of GPS and Leveling Surveys,” *Geophysical Research Letters*, Vol. 24, No. 14, pp. 1839 – 1842. 1997.

Pruess, K.: “TOUGH2 - A General-Purpose Numerical Simulator for Multiphase Fluid and Heat Flow”, Report LBL-29400, *Lawrence Berkeley National Laboratory*, Berkeley Calif. (1991).

Reyes, J.L.P, and Horne, R.N.: “Analysis Of The Geysers Well Field Performance Data to Infer In-Situ Water Saturation,” Proceedings of the GRC 2002 Annual Meeting, September 25-27, 2002, Reno, California, USA; *Geothermal Resources Council* Trans. V. **26** (2002).

Taylor, R.E., Shoemaker, R. L., and Groot, H.: “Thermophysical Properties of Selected Rocks: A Report to U.S.G.S.,” *TPRL* 271 32 pp., Thermophysical Prop. Res. Lab., Purdue Univ., Indiana, 1982.

Walters, M., and Combs, J.: “Heat Flow Regime in the Geysers-Clear Lake Area of Northern California,” *Geothermal Resources Council*, Trans. **14** (1989)

Williamson, K.H.: “Reservoir Simulation of the Geysers Geothermal Field,: *Proceedings*, Fifteenth workshop on Geothermal Reservoir Engineering, Stanford University, California, January 23 – 25, 1990: SGP-TR-130.